Dynamics of domain walls in weak ferromagnets

N. Papanicolaou
Department of Physics, University of Crete, and Research Center of Crete, Heraklion, Greece
(Received 3 September 1996; revised manuscript received 3 December 1996)

The dynamics of domain walls in a model weak ferromagnet is shown to be governed by a suitable extension of the relativistic nonlinear σ model to account for the Dzyaloshinskii-Moriya anisotropy and an applied magnetic field. Our analytical results are confirmed by a numerical calculation in a discrete spin model and significantly amend earlier treatments. Thus we provide a detailed description of static domain walls and subsequently study their dynamics. A virial theorem is derived that underlies the existence of a terminal state and allows a simple calculation of the mobility at low fields for both Bloch and Néel walls. We further establish the existence of a critical field above which a driven domain wall is always Néel, whereas a bifurcation takes place below the critical value where the two types of walls behave rather differently. The terminal states as well as the mobility curves are obtained for practically any strength of the applied field. Implications for the phenomenology of domain walls in orthoferrites and in rhombohedron weak ferromagnets are discussed briefly. [S0163-1829(97)10017-0]

I. INTRODUCTION

Weak ferromagnets (WFM's) are basically antiferromagnets (AFM's) in which a small permanent magnetization arises thanks to an antisymmetric exchange interaction discovered and studied by Dzyaloshinskii[1] and Moriya.[2] An early account of the main properties of weak ferromagnets may be found in the review article of Moriya[3] while a recent book[4] focuses on the dynamics of topological magnetic solitons such as domain walls.

At first sight, it is natural to assume that the situation is similar to that of the extensively studied ferromagnetic (FM) domain walls where the essential dynamical features are captured by an analytical solution derived by Walker.[5] When a FM wall is subjected to an external field h, it reaches a terminal state with constant velocity $v=v(h)$ for field strengths below a certain critical value h_w but undergoes a complicated evolution for $h>h_w$. A related fact is that the maximum velocity achieved by the wall in the region $h<h_w$ is typically small, of the order of a few hundred meters per sec. Although important boundary effects in ferromagnetic films render the Walker solution inapplicable in its details, the overall picture is essentially correct and has been the main source of intuition for many refinements that followed.[6]

However, experimental studies of WFM walls[4] have revealed a significantly different dynamical behavior; no trace of a critical Walker field has been found and the observed wall velocities are typically much greater than those encountered in ferromagnets. Instead of a Walker maximum one observes a limiting velocity c that coincides with the phase velocity of the magnons associated with the underlying antiferromagnetic exchange interaction. As a consequence, the limiting velocity is rather high, reaching the value $c \approx 20$ km/sec in the most typical example of an orthoferrite that exhibits weak ferromagnetism ($YFeO_3$). One may then invoke the simple formula

$$v=\frac{\mu h}{\sqrt{1+(\mu h/c)^2}} \tag{1.1}$$

to interpolate between the expected linear behavior at low fields ($v\approx\mu h$, where μ is the wall mobility) and a limiting velocity ($v\approx c$) in the opposite limit ($h\to\infty$). Formula (1.1) shows no sign of a critical field but is in reasonable agreement with experimental data.[4]

The actual picture in, say, $YFeO_3$ is more involved in that Eq. (1.1) provides only a rough envelop of the experimental curve. The latter is interrupted by at least two plateaus in the vicinity of $v\approx 4$ and 7 km/sec which are identified with the velocities of longitudinal and transverse sound and suggest a resonant coupling between magnetic degrees of freedom and lattice vibrations. Such magnetoelastic anomalies are absent in ordinary ferromagnets because the maximum Walker velocity is usually smaller than the speed of sound. Since the pure WFM wall dynamics already confronts us with a nontrivial problem, magnetoelastic couplings will be neglected in the present work but could be included on a future occasion.

The semiempirical relation (1.1) may be thought of as a relativistic extension of the linear mobility relation $v=\mu h$. Indeed all previous attempts at a theoretical derivation of Eq. (1.1) were based on a phenomenological continuum model that is a generalization of the relativistic nonlinear σ model.[4] On the other hand, our recent study of AFM domain walls[7] suggests that some tricky issues arise in the derivation of a continuum approximation. The first objective of the present paper is then to repeat the analysis of Ref. 7 in the presence of the Dzyaloshinskii-Moriya anisotropy. We shall find that relation (1.1) survives in a subtle and interesting way but it certainly falls short of explaining the whole story. For example, it is tacitly assumed in the work reviewed in Ref. 4 that the terminal velocities of driven Bloch and Néel walls are given by two independent copies of relation (1.1) distinguished only by the respective mobilities. Instead, we find that only Néel walls are described by the simple relativistic formula (1.1) whereas the mobility curve of Bloch walls is significantly different. Nevertheless, a critical field h_c exists above which a driven Bloch wall is dynamically converted into a Néel wall. Above h_c both types of walls are described

by a single mobility curve of type (1.1) applied with a mobility μ appropriate for Néel walls; see Fig. 9 at the end of the paper.

In view of the great diversity as well as crystallographic complexity of realistic weak ferromagnets, it is useful to develop a simple microscopic model that entails only the essential features of the dynamics. In a sense, our aim here is to obtain the analog of the idealized Walker solution. Hence, in Sec. II, we introduce the simplest discrete spin model that embodies the main interactions present in a typical weak ferromagnet. The model is then used to calculate the profile of static domain walls by a relaxation algorithm applied directly on the lattice. The calculated domain walls are reproduced very precisely by analytical solutions derived within the continuum approximation worked out in Sec. III. The same section lays down the foundation for a complete study of the dynamics of driven domain walls, which is carried out in Sec. IV. The main conclusions are summarized in Sec. V and some calculational details are relegated to the Appendix.

II. THE DISCRETE SPIN MODEL

In order to obtain a manageable theoretical framework we consider a strictly one-dimensional (1D) discrete spin model in which magnetic ions are placed on a chain whose sites are labeled by $i=1,2,\ldots,\Lambda$. The spin Hamiltonian consists of three terms,

$$W=W_E+W_{\mathrm{DM}}+W_A, \tag{2.1}$$

corresponding to the exchange, Dzyaloshinskii-Moriya (DM), and single-ion anisotropy contributions. The exchange interaction is taken to be antiferromagnetic, i.e.,

$$W_E=J\sum_i (\mathbf{S}_i\cdot\mathbf{S}_{i+1}), \tag{2.2}$$

with $J>0$, and we consider an antisymmetric DM interaction of the form

$$W_{\mathrm{DM}}=\sum_i (-1)^{i+1}\mathbf{D}\cdot(\mathbf{S}_i\times\mathbf{S}_{i+1}), \tag{2.3}$$

where **D** is a vector of constant direction and magnitude D. A microscopic explanation of the sign alternation present in the sum of Eq. (2.3) may be inferred from the discussion of Moriya[3] and is crucial for the occurrence of weak ferromagnetism. Lack of sign alternation would instead lead to a spiral spin state.

A strictly 1D model describes fairly well rhombohedron weak ferromagnets such as $MnCO_3$ where the magnetic Mn ions interact significantly only along the crystallographic c axis.[8] Between any two successive Mn ions on the c axis there exists a CO_3 complex such that the relative orientation of the triangle formed by the three oxygen atoms alternates at any two successive bonds, in direct correspondence with the sign alternation in Eq. (2.3). This example suggests the more abstract notation[9] employed in the first row of Fig. 1 to illustrate a short chain where open circles stand for the magnetic ions and up (down) triangles located on the bonds indicate positive (negative) signs in the sum (2.3).

It would be natural to pursue the discussion of the above example through to its conclusion. However, rhombohedron

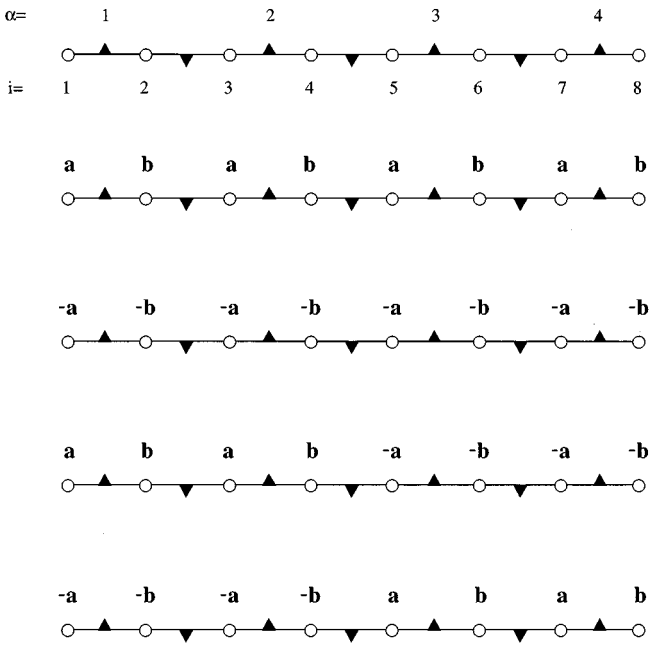

FIG. 1. Illustration on a short chain of labeling conventions and the dimerization process (first row), of the two degenerate ground states (second and third rows), and of the two types (antikink and kink) of prototype domain walls (fourth and fifth rows).

weak ferromagnets are characterized by a sixth-order single-ion anisotropy in the basal plane which would technically complicate the theoretical development. We thus prefer to complete our model by considering instead the most general rhombic anisotropy

$$W_A=\frac{1}{2}\sum_i [g_1(S_i^1)^2+g_2(S_i^2)^2+g_3(S_i^3)^2], \tag{2.4}$$

where S_i^1, S_i^2, and S_i^3 are the Cartesian components of spin along the principal axes and g_1, g_2, and g_3 are anisotropy constants.

Actually a rhombic anisotropy is suitable for the study of orthoferrites such as $YFeO_3$. But a strictly 1D model is not directly relevant in this case because the interacting magnetic Fe ions form a 3D lattice.[10] Recall, however, that domain walls are 1D structures embedded in a crystal in such a way that substantial variations of spin occur along a single direction. Therefore, when a continuum approximation is applicable, domain walls are effectively described by a differential equation that is formulated in terms of a single spatial variable in addition to time. In such a context all memory of the original lattice is reflected in appropriate renormalizations of the microscopic parameters by simple functions of the coordination number. Hence we shall assume that the 1D discrete spin model applies to the domain-wall dynamics of orthoferrites, with due caution on the determination of the relevant microscopic parameters. Some indirect conclusions will also be drawn for rhombohedron weak ferromagnets.

Within the limits of the 1D model the chain direction need not coincide with any of the principal axes used for the specification of the anisotropy constants in Eq. (2.4). In other words, spin rotations act as an internal group without specific reference to a coordinate system in real space. In order to

keep with the interpretation alluded to in the preceding paragraph we will adopt the real-space conventions commonly used in discussions of orthoferrites[4,10] but the direction of the chain will be left arbitrary. We introduce the unit vectors $\mathbf{e}_1=(1,0,0)$, $\mathbf{e}_2=(0,1,0)$, and $\mathbf{e}_3=(0,0,1)$ along the three principal axes and take the constant vector $\mathbf{D}$ to point along the second axis: $\mathbf{D}=D\mathbf{e}_2$. Spins will be treated as classical vectors with constant magnitude s, $\mathbf{S}_i^2=s^2$, which is a simple multiple of the Planck constant; e.g., $s=\frac{5}{2}\hbar$ for the Fe ions in $YFeO_3$. Because of this constraint one of the anisotropy constants may be set equal to zero, e.g., $g_1=0$, without loss of generality. The remaining constants g_2 and g_3 are often taken to be equal and positive, a choice that leads to a uniaxial anisotropy with the easy axis in the first direction. The restriction of equal magnitudes will not be made in the present work but we will assume for the moment that both g_2 and g_3 are positive so that the first axis is still the easy axis.

Thus we are ready to address the first important question concerning the nature of the ground state. If the DM anisotropy were absent ($D=0$) the minimum energy configuration would be the usual Néel state with spins polarized along the first axis. For $D\neq 0$, the ground state is also achieved with spins alternating between two distinct values. In the notation of Fig. 1 all spins to the left of an up triangle take the value $\mathbf{A}$ and those to the right of such a triangle the value $\mathbf{B}$. In terms of the corresponding unit vectors $\mathbf{a}=\mathbf{A}/s$ and $\mathbf{b}=\mathbf{B}/s$ the energy per site measured in units of s^2J, i.e., $w=W/s^2J\Lambda$, is given by

$$w=(\mathbf{a}\cdot\mathbf{b})+\frac{1}{J}\,\mathbf{D}\cdot(\mathbf{a}\times\mathbf{b})+\frac{g_2}{4J}\,(a_2^2+b_2^2)+\frac{g_3}{4J}\,(a_3^2+b_3^2). \tag{2.5}$$

The sign alternation present in Eq. (2.3) is crucial for the validity of Eq. (2.5) and for the implied repetition of the pair $(\mathbf{a},\mathbf{b})$ along the chain. Now the energy (2.5) is minimized by the two distinct canted spin configurations shown in Fig. 2, which lie in the (13) plane and are related to each other by the parity transformation $(\mathbf{a},\mathbf{b})\rightarrow(-\mathbf{a},-\mathbf{b})$. In both cases the energy is given by

$$w=-\cos 2\delta-\frac{D}{J}\sin 2\delta+\frac{g_3}{4J}\,(1-\cos 2\delta), \tag{2.6}$$

and the canting angle δ is found by minimizing Eq. (2.6) to obtain

$$\tan 2\delta=\frac{D}{J+g_3/4}. \tag{2.7}$$

Figure 2 also depicts the two vectors

$$\mathbf{m}=\frac{1}{2}\,(\mathbf{a}+\mathbf{b}),\quad \mathbf{n}=\frac{1}{2}\,(\mathbf{a}-\mathbf{b}), \tag{2.8}$$

which will play a special role in the following. These vectors may be expressed in terms of the canting angle as

$$\mathbf{m}=\pm(0,0,\sin\delta),\quad \mathbf{n}=\pm(\cos\delta,0,0), \tag{2.9}$$

where the $\pm$ choice corresponds to the two degenerate ground states shown in Fig. 2. The vector $\mathbf{m}$ may be interpreted as the magnetization and is seen to assume a nonvanishing value, hence leading to weak ferromagnetism.

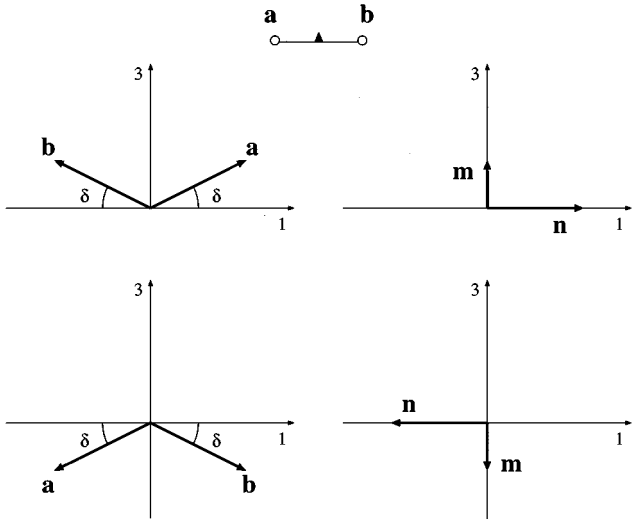

FIG. 2. The two degenerate ground states in the absence of an external field, which are related to each other by the parity transformation $(\mathbf{a},\mathbf{b})\rightarrow(-\mathbf{a},-\mathbf{b})$.

The two types of ground states described above are shown schematically in the second and third rows of Fig. 1, in preparation for the definition of the prototype domain walls given in the fourth and fifth rows of the same figure. By convention, these configurations will be referred to as antikink and kink and correspond to the two distinct ways of connecting the two degenerate ground states between the two ends of the chain. More general domain-wall configurations may be constructed on long chains by retaining the asymptotic characteristics of the prototype walls while choosing the intermediate spin values more or less at random.

However our aim here is to obtain true domain walls that are local minima of the energy functional and are thus stable spin configurations, even though their energy is greater than the energy of the ground state. It is then important to consider the dynamics associated with the Hamiltonian (2.1)–(2.4). The equation of motion for the spin vector $\mathbf{S}_i$ treated as classical may be put in the standard Landau-Lifshitz form

$$\frac{\partial\mathbf{S}_i}{\partial t}=\mathbf{S}_i\times\mathbf{F}_i,\quad \mathbf{S}_i^2=s^2, \tag{2.10}$$

where the effective field $\mathbf{F}_i$ is given by the general relation

$$\mathbf{F}_i=-\frac{\partial W}{\partial\mathbf{S}_i}, \tag{2.11}$$

or, more explicitly, by

$$\mathbf{F}_i=-J(\mathbf{S}_{i+1}+\mathbf{S}_{i-1})-(-1)^i\mathbf{D}\times(\mathbf{S}_{i+1}+\mathbf{S}_{i-1})$$
$$-g_1S_i^1\mathbf{e}_1-g_2S_i^2\mathbf{e}_2-g_3S_i^3\mathbf{e}_3. \tag{2.12}$$

Our first concern is to search for static solutions which satisfy Eq. (2.10) with the time derivative absent. It is a straightforward matter to verify explicitly that the ground-state configurations may be viewed as the simplest static

solutions. Nontrivial solutions are difficult to obtain analytically but their existence is guaranteed by the following arguments. Note that the prototype domain walls do not solve Eq. (2.10) thanks to the obstruction created at the interface. (This situation is slightly different from the case of pure AFM walls studied in Ref. 7.) Therefore, if a prototype wall is somehow created, it will evolve according to Eq. (2.10) in a complicated precessional mode. Nevertheless, if some dissipation is at work, it will eventually relax in a spin configuration that solves the static equation and is a local minimum of the energy functional. This minimum inherits the topological structure of the prototype wall and is thus distinct from the absolute ground-state minimum.

The preceding remarks also suggest a simple numerical method for the calculation of static domain walls through a relaxation algorithm described in Ref. 7. At this point one must specify the parameters employed in the numerical calculation. The spin magnitude s and the exchange constant J can be scaled out of static solutions and the only relevant parameters are the dimensionless ratios formed by scaling the DM and single-ion anisotropy constants with the exchange constant. These ratios are chosen to belong to a parameter regime that is appropriate for orthoferrites but no special effort is made at this stage to select constants that correspond precisely to a specific substance. Hence we adopt the values $D/J=10^{-2}$, $g_1=0$, $g_2/J=10^{-4}=g_3/J$ in all numerical calculations and consider other possibilities on the basis of analytical solutions derived in subsequent sections. The small canting angle calculated from Eq. (2.7), namely $2\delta\approx 0.57°$, is typical of orthoferrites. To complete the discussion of parameters we introduce the equivalent set $g_1=0$ and

$$\varepsilon=\sqrt{\frac{g_3}{J}},\quad \rho^2=\frac{g_2}{g_3},\quad d=\frac{D}{\varepsilon J}, \tag{2.13}$$

whose theoretical significance will become apparent as the discussion progresses. In our standard numerical example, $\varepsilon=10^{-2}$, $\rho=1$, and $d=1$.

The numerical calculation was performed on an open chain with an even total number of sites $\Lambda=2N$ where N is also even; these are technical assumptions of no great significance and will be commented upon at later stages. We consider only the antikink configuration illustrated for a small ($\Lambda=8$) chain in the fourth row of Fig. 1, the discussion of the kink being completely analogous. The initial (prototype) wall was prepared by assigning the pair of spin values $(\mathbf{a},\mathbf{b})$ throughout the first half of the chain and the pair $(-\mathbf{a},-\mathbf{b})$ on the second half. This configuration was then used as initial condition in the relaxation algorithm of Ref. 7 applied for an effective field $\mathbf{F}_i$ now given by Eq. (2.12). The resulting relaxed state is a static domain wall whose interface spreads out to a (half) width given roughly by $1/\varepsilon=100$ sites, where $\varepsilon=10^{-2}$ is the parameter introduced in Eq. (2.13). To avoid interference from the boundaries the total number of sites must satisfy the inequality $\Lambda\gg 1/\varepsilon$. In our calculation we used a long chain with $\Lambda=5000$ sites in which domain walls fit quite comfortably.

Because of the implicit antiferromagnetic discontinuity of the spin values as one moves from site to site, presenting the explicit results in a concise fashion is in itself an interesting exercise. Anticipating the discussion of the continuum approximation in Sec. III we search for variables that may possess a smooth continuum limit at least in some regions of the parameter space. Thus the $\Lambda=2N$ sites of the chain are grouped into dimers labeled by a sublattice index $\alpha=1,2,\ldots,N$ as illustrated in the first row of Fig. 1. This mode of dimerization is not unique in that every dimer contains a bond that carries an up triangle. Discussion of the dual dimerization in which all dimers contain down triangles is deferred for the moment. Now it is convenient to relabel the two spins contained in the αth dimer according to

$$\mathbf{S}_{2\alpha-1}=\mathbf{A}_\alpha,\quad \mathbf{S}_{2\alpha}=\mathbf{B}_\alpha. \tag{2.14}$$

The advantage of the new spin variables $\mathbf{A}_\alpha$ and $\mathbf{B}_\alpha$ is that each one of them is expected to be smooth as the index α moves from one discrete value to the next. An even more convenient set is provided by the two linear combinations[4]

$$\mathbf{m}_\alpha=\frac{1}{2s}(\mathbf{A}_\alpha+\mathbf{B}_\alpha),\quad \mathbf{n}_\alpha=\frac{1}{2s}(\mathbf{A}_\alpha-\mathbf{B}_\alpha) \tag{2.15}$$

which satisfy the constraints

$$\mathbf{m}_\alpha\cdot\mathbf{n}_\alpha=0,\quad \mathbf{m}_\alpha^2+\mathbf{n}_\alpha^2=1. \tag{2.16}$$

The idea is simply to present the numerical data for the variables $\mathbf{m}_\alpha$ and $\mathbf{n}_\alpha$ as histograms calculated at $\alpha=1,2,\ldots,N$. As it turns out, these histograms approach continuous curves at small values of the parameter ε introduced in Eq. (2.13). We may then drop the index α in the vectors $\mathbf{m}$ and $\mathbf{n}$ and plot their three components as functions of the position variable

$$\xi=2\varepsilon(\alpha-\alpha_0),\quad \alpha=1,2,\ldots,N, \tag{2.17}$$

joining discrete points in the graph by the graphics routine. Here α_0 is an arbitrary constant that sets the origin of the coordinate system. Nevertheless, it is convenient to set the origin at the center of the domain wall which coincides in the present calculation with the center of the open chain and hence $\alpha_0=(N+1)/2$. The resulting graphs are shown in Fig. 3 and make it apparent that a smooth continuum limit has indeed been reached for the small value $\varepsilon=10^{-2}$ used in the numerical calculation.

It is clear that both $\mathbf{m}$ and $\mathbf{n}$ exhibit a more or less standard domain-wall structure. A closer look at the numerical data reveals that the vectors $\mathbf{m}$ and $\mathbf{n}$ quickly approach constant values far from the wall center which are in excellent agreement with the ground-state values (2.9) calculated with a canting angle δ derived from Eq. (2.7). Also note that the components of $\mathbf{m}$ and $\mathbf{n}$ along the second axis vanish. In other words, spins are confined in the (13) plane in order to optimize the energy cost imparted by the DM anisotropy. In the context of orthoferrites such configurations are called ac or Bloch domain walls.[4]

The numerical calculation just presented accomplishes the main goal of this section but its content cannot be fully appreciated before we tie some loose ends. First we return to the use of an open chain with an even total number of sites $\Lambda=2N$ where N is also even. Once a domain wall has been realized on the open chain, removing one or more spins from either side and reiterating the relaxation algorithm would af-

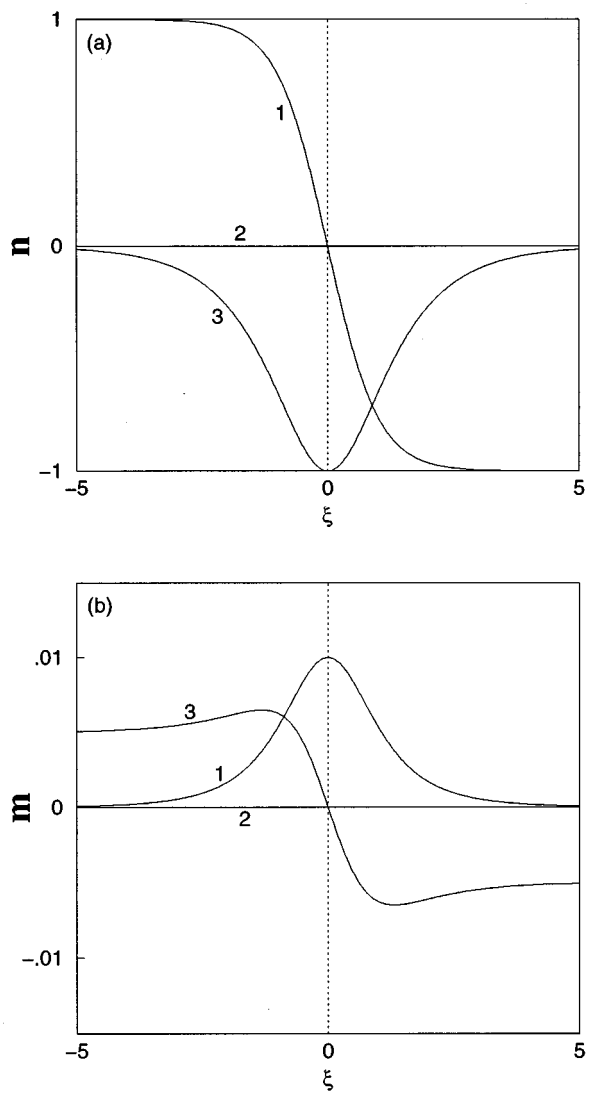

FIG. 3. The profile of a static domain wall calculated numerically within the discrete spin model. The numerical results are presented using the standard dimerization scheme discussed in the text and are very accurately reproduced by the continuum solution (3.30) and (3.31) for a static Bloch wall applied for $\varepsilon=10^{-2}$, $d=1$, and $\kappa=-1=\nu$.

fect the wall only mildly provided that $\Lambda \gg 1/\varepsilon$. In particular, the wall need not be located at the center of the chain, as long as it stays sufficiently appart from the end points, nor does its center have to coincide with the middle of a bond. On the contrary, when we study the dynamics, we shall extensively deal with domain walls that glide through the lattice.

The possible occurrence of interesting surface states around the end points of the chain, which may or may not be related to domain walls, is a separate issue that is not studied in the present paper. This issue has recently attracted considerable attention within the pure AFM model applied to a Fe/Cr superlattice.[11,12] One can only expect that adding to the model the DM anisotropy would lead to a more involved picture.

Yet we must address an apparent ''ambiguity'' that is not related to the size of the chain but rather to the process of dimerization. The best way to illustrate the question is to present the *same* numerical data as those employed in Fig. 3 in conjunction with the dual dimerization where all dimers contain down triangles. Specifically, we simply omit the two end points of the chain and consider the dimers (23), (45), . . . , $(\Lambda-2,\Lambda-1)$ labeled consecutively by an integer $\beta=1,2,\ldots,N-1$. We then construct the fields

$$\mathbf{m}_\beta=\frac{1}{2s}(\mathbf{S}_{2\beta}+\mathbf{S}_{2\beta+1}),\quad \mathbf{n}_\beta=\frac{1}{2s}(\mathbf{S}_{2\beta}-\mathbf{S}_{2\beta+1}), \tag{2.18}$$

which are the direct analogs of Eq. (2.15) in the dual dimerization scheme. We again consider the histograms for $\mathbf{m}_\beta$ and $\mathbf{n}_\beta$ by plotting the data as functions of the variable

$$\xi=2\varepsilon(\beta-\beta_0),\quad \beta=1,2,\ldots,N-1, \tag{2.19}$$

with discrete points joined smoothly through the graphics routine. Here we may set the origin of the coordinate system at the center of the wall by choosing the arbitrary constant as $\beta_0=N/2$. The resulting curves are shown in Fig. 4 and should be compared to those of Fig. 3.

The observed significant differences between the two figures are at first disturbing. However a closer examination reveals that these differences are quite natural and, indeed, necessary for the consistency of the entire calculation. For example, the field **n** has flipped sign and now appears as a kink configuration in contrast to the antikink of Fig. 3. On the other hand, the asymptotic values of **m** and **n** must now be given by

$$\mathbf{m}=\frac{1}{2}(\mathbf{b}+\mathbf{a}),\quad \mathbf{n}=\frac{1}{2}(\mathbf{b}-\mathbf{a}), \tag{2.20}$$

instead of the values (2.8) in the original dimerization. Therefore, the necessity of a sign flip in the field **n** becomes self-evident at least in the asymptotic region. The same argument suggests that the asymptotic values of the field **m** must remain the same, as actually observed in Figs. 3 and 4, or that the kink (antikink) character of **m** is preserved. The last statement could have been anticipated on physical grounds, for a nonvanishing **m** in the ground state signals the occurrence of (weak) ferromagnetism and cannot depend on the mathematical process of dimerization.

Nevertheless, no such simple explanation of the observed curious differences around the wall center can be given until a complete analytical solution is obtained within the continuum approximation in Sec. III. At this point we merely state that the answer to any physically relevant question is independent of the specific mode of dimerization, provided that the mathematical framework is not overinterpreted. For instance, if **m** is interpreted literally as magnetization, one may wonder whether Fig. 3 or Fig. 4 will describe the results of an actual measurement. In fact, either figure can be used as long as experimental resolution is such that spin values can be measured at every site. Otherwise, one should expect to observe a fuzzy magnetization curve around the wall center, which becomes progressively sharper as one moves away from the wall where the field **m** attains definite values that are independent of the mode of dimerization.

A number of physically relevant questions will be asked and answered unambiguously in the continuation of the pa-

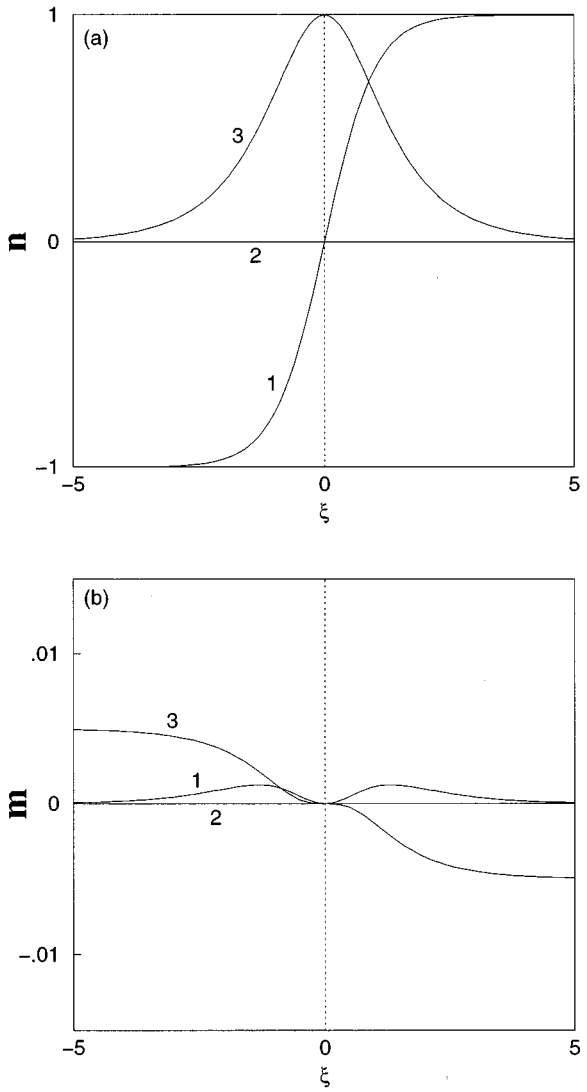

FIG. 4. The same numerical results as those of Fig. 3 now presented using the dual dimerization scheme and very accurately reproduced by the continuum solution (3.30) and (3.31) applied for $\varepsilon = 10^{-2}$, $d = -1$, and $\kappa = 1 = \nu$.

per. This section is concluded by recalling an example of such a question that was posed within the pure AFM model in Ref. 7. At small ε, AFM domain walls acquire a nonvanishing total magnetic moment equal to $\pm s$ with respect to the ground state. However, it is impossible to ascertain where the moment of a pure AFM wall is actually located, in view of the fact that the local values of **m** are sensitive to the mode of dimerization; in this respect, the result of Ref. 7 was overstated. Nevertheless the total moment is unambiguously defined on any finite chain irrespectively of the mode of dimerization, the latter being only a technique for obtaining a continuum approximation. Specifically, let us return to a domain wall of the type shown schematically in Fig. 1 of Ref. 7 on a long finite chain with an even number of sites $\Lambda = 2N$. Such a wall carries a total moment s at sufficiently weak anisotropy, whereas a wall with total moment $-s$ can be obtained on the *same* chain by reversing the signs of all spins. Now suppose that one removes both the leftmost and the rightmost spin of the original configuration, a move that amounts to reducing the total moment by $2s$. The spin configuration on the reduced chain is now a domain wall with total moment $-s$. But a wall with total moment s also exists on the reduced chain and is again obtained by reversing the signs of all spins. Therefore for any finite chain with an even number of sites domain walls develop a net moment $\pm s$ while the moment of the ground state vanishes. The last remark is pertinent to the possibility of removing only one spin from either side of the chain. The resulting spin configuration carries a vanishing total moment, but the ground state of the reduced chain with an odd number of sites $\Lambda - 1 = 2N - 1$ is now doubly degenerate and carries a moment either s or $-s$. Hence the total moment of the domain wall again differs from that of either ground state by an amount $-s$ or s.

The above examples strengthen the earlier conclusion that the tiny wall moment $\pm s$ is not localized and is to some extent elusive. Therefore such a moment is hardly relevant for macroscopic properties, such as those discussed in the present paper, but could be important in, say, a semiclassical quantization of pure AFM domain walls in a quantum antiferromagnetic chain.[13] The process of dimerization, or any other substitute, is an inevitable fact of life in the derivation of a continuum approximation for antiferromagnets. It is then important that the continuum model derived in the following section cope with apparent paradoxes, as is discussed further after Eq. (3.33).

III. THE NONLINEAR σ MODEL

The numerical calculation of static domain walls in the discrete spin model makes it clear that a suitable continuum approximation should be possible to obtain in some region of the parameter space. The appropriate region is actually suggested by the specific choice made in Sec. II. Indeed a relatively simple continuum model emerges for parameters such that $g_1 = 0$ and

$$\frac{D}{J}, \frac{g_2}{J}, \frac{g_3}{J} \ll 1. \tag{3.1}$$

These inequalities are generally satisfied in realistic weak ferromagnets and will be invoked in the following without exception. We must also consider the effects of an externally applied field as well as dissipation. The latter is taken to be of the standard Landau-Gilbert form and Eq. (2.10) is further extended to include the effect of a uniform magnetic field **H**,

$$\frac{\partial \mathbf{S}_i}{\partial t} + \gamma\left(\mathbf{S}_i \times \frac{\partial \mathbf{S}_i}{\partial t}\right) = \mathbf{S}_i \times (\mathbf{F}_i + g_0 \mu_0 \mathbf{H}), \tag{3.2}$$

where γ is the dissipation constant, $g_0 \sim 2$ is the gyromagnetic ratio, and $\mu_0 = e/2m_e c$ is the Bohr magneton divided by the Planck constant. In our conventions the combinations of parameters $s\gamma$ and $g_0\mu_0 H/sJ$ are dimensionless and may assume any values within the discrete spin model. However, for the validity of a continuum description, inequalities (3.1) must be supplemented by

$$s\gamma, \frac{g_0 \mu_0 H}{sJ} \ll 1, \tag{3.3}$$

which are sufficiently nonstringent for all practical purposes. More convenient rationalized quantities are defined by

$$\lambda=\frac{2s\gamma}{\varepsilon},\quad \mathbf{h}=\frac{g_0\mu_0\mathbf{H}}{2\varepsilon sJ}, \tag{3.4}$$

and extend the set of parameters introduced in Eq. (2.13). Inequalities (3.1) and (3.3) then read

$$\varepsilon,\varepsilon\rho,\varepsilon d,\varepsilon\lambda,\varepsilon h\ll 1 \tag{3.5}$$

and are conditions for the validity of the continuum model derived in this section.

The continuum model is derived by a method already employed in the simpler context of Ref. 7. We adopt the dimerization scheme of Fig. 1 and again defer discussion of the dual dimerization. The Landau-Lifshitz equation (3.2) is then rewritten as a system of two coupled equations for the sublattice spins $\mathbf{A}_\alpha$ and $\mathbf{B}_\alpha$ introduced in Eq. (2.14):

$$\begin{aligned}\frac{\partial\mathbf{A}_\alpha}{\partial t}+\gamma\left(\mathbf{A}_\alpha\times\frac{\partial\mathbf{A}_\alpha}{\partial t}\right)&=\mathbf{A}_\alpha\times(\mathbf{F}_\alpha+g_0\mu_0\mathbf{H}),\\ \frac{\partial\mathbf{B}_\alpha}{\partial t}+\gamma\left(\mathbf{B}_\alpha\times\frac{\partial\mathbf{B}_a}{\partial t}\right)&=\mathbf{B}_\alpha\times(\mathbf{G}_\alpha+g_0\mu_0\mathbf{H}),\end{aligned} \tag{3.6}$$

where the effective fields $\mathbf{F}_\alpha$ and $\mathbf{G}_\alpha$ are given by

$$\begin{aligned}\mathbf{F}_\alpha&=-J(\mathbf{B}_{\alpha-1}+\mathbf{B}_\alpha)+\mathbf{D}\times(\mathbf{B}_{\alpha-1}+\mathbf{B}_\alpha)\\&\quad-g_1A_\alpha^1\mathbf{e}_1-g_2A_\alpha^2\mathbf{e}_2-g_3A_\alpha^3\mathbf{e}_3,\\ \mathbf{G}_\alpha&=-J(\mathbf{A}_\alpha+\mathbf{A}_{\alpha+1})-\mathbf{D}\times(\mathbf{A}_\alpha+\mathbf{A}_{\alpha+1})\\&\quad-g_1B_\alpha^1\mathbf{e}_1-g_2B_\alpha^2\mathbf{e}_2-g_3B_\alpha^3\mathbf{e}_3.\end{aligned} \tag{3.7}$$

A sign alternation is no longer present in the DM contributions but its effect has been correctly accounted for in Eqs. (3.7) in relation to the specific mode of dimerization.

The main assumption supported by the numerical data is that the sublattice spins $\mathbf{A}_\alpha$ and $\mathbf{B}_\alpha$ approach smooth continuum limits $\mathbf{A}=\mathbf{A}(\xi)$ and $\mathbf{B}=\mathbf{B}(\xi)$ where ξ is the discrete variable (2.17) that becomes continuous in the limit $\varepsilon\to 0$. The dimensionless variable ξ provides a measure of position along the original chain. The actual distance on the chain is given by $a\xi/\varepsilon$ where a is the physical distance between two magnetic ions. However the lattice constant a will not be used in any stage of the theoretical development except when quantities such as distance, velocity, etc., will have to be translated in physical units. Thus we make the replacements $\mathbf{A}_\alpha\to\mathbf{A}$ and $\mathbf{B}_\alpha\to\mathbf{B}$ in Eqs. (3.6) and (3.7) together with

$$\begin{aligned}\mathbf{A}_{\alpha+1}&\to\mathbf{A}+(2\varepsilon)\mathbf{A}'+\frac{1}{2}(2\varepsilon)^2\mathbf{A}'',\\ \mathbf{B}_{\alpha-1}&\to\mathbf{B}-(2\varepsilon)\mathbf{B}'+\frac{1}{2}(2\varepsilon)^2\mathbf{B}'',\end{aligned} \tag{3.8}$$

where the prime denotes differentiation with respect to ξ.

Subsequent steps of the argument differ from those of Ref. 7 only in the length of the required algebra and will be relegated to the Appendix to avoid obscurring the simplicity of the final result. Let us consider the continuum analogs of the fields (2.15), i.e.,

$$\mathbf{m}=\frac{1}{2s}(\mathbf{A}+\mathbf{B}),\quad \mathbf{n}=\frac{1}{2s}(\mathbf{A}-\mathbf{B}), \tag{3.9}$$

and introduce the rescaled time variable

$$\tau=2\varepsilon sJt. \tag{3.10}$$

We further recall the set of parameters $g_1=0$, ε, ρ, and d of Eq. (2.13), which we extend slightly by defining a vector $\mathbf{d}$ whose magnitude is equal to d and its direction coincides with the DM axis ($\mathbf{d}=d\mathbf{e}_2$), and the rationalized dissipation constant λ and field $\mathbf{h}$ of Eq. (3.4).

In the strict continuum limit m and n satisfy the reduced constraints

$$\mathbf{m}\cdot\mathbf{n}=0,\quad \mathbf{n}^2=1, \tag{3.11}$$

$\mathbf{m}$ is expressed entirely in terms of $\mathbf{n}$ as

$$\mathbf{m}=\frac{\varepsilon}{2}[-\mathbf{n}'+(\mathbf{n}\times\dot{\mathbf{n}})+(\mathbf{n}\times\mathbf{d})-\mathbf{n}\times(\mathbf{n}\times\mathbf{h})], \tag{3.12}$$

and the field $\mathbf{n}$ satisfies the differential equation

$$\mathbf{n}\times(\mathbf{f}+\lambda\dot{\mathbf{n}})=0, \tag{3.13}$$

where we have separated the dissipative term and the effective field $\mathbf{f}$ reads

$$\begin{aligned}\mathbf{f}&=\ddot{\mathbf{n}}-\mathbf{n}''+2(\mathbf{h}\times\dot{\mathbf{n}})+(\mathbf{h}\times\mathbf{d})+(\mathbf{n}\cdot\mathbf{h})\mathbf{h}+(\mathbf{n}\cdot\mathbf{d})\mathbf{d}\\&\quad+\rho^2n_2\mathbf{e}_2+n_3\mathbf{e}_3.\end{aligned} \tag{3.14}$$

The dot stands for differentiation with respect to the time variable τ of Eq. (3.10) and the prime with respect to the spatial variable ξ of Eq. (2.17). It is understood that the strong inequalities (3.5) are enforced and terms of order ε^2 and higher have been neglected.

Therefore the ''magnetization'' $\mathbf{m}$ may be viewed as an auxiliary field and the dynamics is governed mainly by Eq. (3.13) at the heart of which lies the relativistic nonlinear σ model. The latter corresponds to the first two terms of the effective field $\mathbf{f}$ which originate in the pure antiferromagnetic interaction. The fifth and sixth terms amount to a redefinition of the anisotropy constants due to the applied field and the DM interaction. The third term in $\mathbf{f}$ is special in that it breaks Lorentz invariance at nonvanishing field, whereas the term $(\mathbf{h}\times\mathbf{d})$ introduces a direct coupling between the applied field and the DM anisotropy.

In order to facilitate a direct comparison to the early work it is also useful to derive the effective field from an action principle,

$$\mathbf{f}=-\frac{\delta\mathcal{A}}{\delta\mathbf{n}}, \tag{3.15}$$

where $\mathcal{A}$ is the action

$$\mathcal{A}=\int L\,d\xi\,d\tau \tag{3.16}$$

and L the corresponding Lagrangian density:

$$L=\frac{1}{2}(\dot{\mathbf{n}}^2-\mathbf{n}'^2)+\mathbf{h}\cdot(\mathbf{n}\times\dot{\mathbf{n}})-(\mathbf{h}\times\mathbf{d})\cdot\mathbf{n}$$

$$-\frac{1}{2}[(\mathbf{n}\cdot\mathbf{h})^2+(\mathbf{n}\cdot\mathbf{d})^2+\rho^2 n_2^2+n_3^2]. \qquad (3.17)$$

This result agrees for the most part with Eq. (2.30) of Ref. 4 (restricted to an antisymmetric DM interaction) with the important exception of the crossed term $-(\mathbf{h}\times\mathbf{d})\cdot\mathbf{n}$ which is absent in the above reference; so is a parity-breaking gradient term in Eq. (2.28) of the same reference. It should be mentioned here that the possible existence of a parity-breaking contribution in the field $\mathbf{m}$ had been anticipated on symmetry grounds[14] but such a possibility was apparently overlooked in the literature for a long time.[7,13] This contribution is sensitive to the symmetry of the lattice and may be special to the model considered here. But it should also be clear that the crossed term $(\mathbf{h}\times\mathbf{d})$ in the effective field $\mathbf{f}$ is not related to the parity-breaking contribution and its consequences are more drastic for the dynamics of domain walls. The implications of these differences will be discussed in the following as the need arises.

Before proceeding with detailed applications of the derived continuum model we must comment on the rationalized physical units employed throughout this paper. The spin magnitude s carries dimension of action, sJ of frequency, and s^2J of energy. The constants s and J as well as the lattice constant a do not appear explicitly in the dynamical equations which are formulated in terms of the dimensionless ratios ε, ρ, d, λ, and h. In particular, the spatial coordinate ξ of Eq. (2.17) and the time variable τ of Eq. (3.10) are both dimensionless. A related fact is that the ''velocity of light'' associated with Eq. (3.14) is equal to unity. Recalling that the actual distance on the chain is given by $a\xi/\varepsilon$ and taking into account the definition of time in Eq. (3.10) we conclude that velocity is measured in units of

$$c=2asJ, \qquad (3.18)$$

which coincides with the phase velocity of magnons in the long-wavelength limit of the underlying pure 1D antiferromagnet and also provides an expression for the limiting velocity c discussed in the Introduction. On this occasion, we wish to return to our earlier remarks concerning the use of the 1D model in relation to orthoferrites. The rationalized continuum equations of the field $\mathbf{n}$ for the description of domain walls within the 3D crystal will have the same form as those derived above but the interpretation of constants will be slightly different. For instance, the limiting velocity is given more generally by

$$c=2asJ\sqrt{\frac{z}{2}}, \qquad (3.19)$$

where z is the lattice coordination number.

As a first application of the continuum model we consider the derivation of static domain walls at vanishing field. One may then neglect field-dependent terms as well as time derivatives in Eqs. (3.12)–(3.14) and further insert the special form of the vector $\mathbf{d}=d\mathbf{e}_2$ to obtain

$$\mathbf{m}=\frac{\varepsilon}{2}[-\mathbf{n}'+d(\mathbf{n}\times\mathbf{e}_2)] \qquad (3.20)$$

and

$$\mathbf{n}\times\mathbf{f}=0, \quad \mathbf{f}=-\mathbf{n}''+(d^2+\rho^2)n_2\mathbf{e}_2+n_3\mathbf{e}_3. \qquad (3.21)$$

It proves useful to rewrite the effective field $\mathbf{f}$ in the abstract form

$$\mathbf{f}=\frac{\delta\mathcal{F}}{\delta\mathbf{n}}, \qquad (3.22)$$

where $\mathcal{F}$ is an energy functional given by

$$\mathcal{F}=\frac{1}{2}\int[\mathbf{n}'^2+(d^2+\rho^2)n_2^2+n_3^2]d\xi. \qquad (3.23)$$

Resolving the constraint $\mathbf{n}^2=1$ by the standard spherical parametrization,

$$n_1=\sin\Theta\cos\Phi, \quad n_2=\sin\Theta\sin\Phi, \quad n_3=\cos\Theta, \qquad (3.24)$$

yields

$$\mathcal{F}=\frac{1}{2}\int[\Theta'^2+\sin^2\Theta\Phi'^2+(d^2+\rho^2)$$
$$\times\sin^2\Theta\sin^2\Phi+\cos^2\Theta]d\xi, \qquad (3.25)$$

and static solutions are stationary points of $\mathcal{F}$ with respect to Θ and Φ. Hence we are led to the system of ordinary differential equations

$$\Theta''+[1-\Phi'^2-(d^2+\rho^2)\sin^2\Phi]\cos\Theta\sin\Theta=0,$$
$$(\sin^2\Theta\Phi')'=(d^2+\rho^2)\sin^2\Theta\cos\Phi\sin\Phi. \qquad (3.26)$$

Bloch domain walls are confined in the (13) plane and thus satisfy the simpler system

$$\Phi=0, \quad \Theta''+\cos\Theta\sin\Theta=0, \qquad (3.27)$$

whose solution reads

$$\sin\Theta=\kappa\tanh\xi, \quad \cos\Theta=\frac{\nu}{\cosh\xi}, \qquad (3.28)$$

where the ''kink number'' κ and the ''polarity'' ν are given by

$$\kappa=\pm1, \quad \nu=\pm1, \qquad (3.29)$$

taken in any combination. Therefore the vector $\mathbf{n}=(n_1,n_2,n_3)$ is given explicitly by

$$n_1=\kappa\tanh\xi, \quad n_2=0, \quad n_3=\frac{\nu}{\cosh\xi}, \qquad (3.30)$$

and the corresponding expressions for $\mathbf{m}=(m_1,m_2,m_3)$ are calculated from Eq. (3.20) using as input Eq. (3.30):

$$m_1 = -\frac{\varepsilon}{2\cosh\xi}\left(\frac{\kappa}{\cosh\xi}+\nu d\right),$$

$$m_2 = 0,$$

$$m_3 = \frac{\varepsilon}{2}\tanh\xi\left(\frac{\nu}{\cosh\xi}+\kappa d\right). \tag{3.31}$$

Applied for $\varepsilon = 10^{-2}$, $d=1$, and $\kappa=-1=\nu$ the above continuum approximation is found to be graphically indistinguishable from the numerical solution of Fig. 3. A good estimate of the relative accuracy is already given by the asymptotic values of the fields (3.30) and (3.31) evaluated at $\xi=\pm\infty$:

$$\mathbf{m}(\pm\infty) = \pm\kappa(0,0,\varepsilon d/2), \quad \mathbf{n}(\pm\infty) = \pm\kappa(1,0,0). \tag{3.32}$$

For the specific numerical example, Eq. (3.26) yields $\mathbf{m}(\pm\infty) = \mp(0,0,0.005)$ and $\mathbf{n}(\pm\infty) = \mp(1,0,0)$ which are consistent with the accurate values given in Eq. (2.9). More generally, for parameters satisfying the inequalities (3.1), the canting angle of Eq. (2.7) may be approximated by $\delta \approx D/2J = \varepsilon d/2$ and Eq. (3.32) is consistent with Eq. (2.9) applied for $\sin\delta\approx\delta$ and $\cos\delta\approx 1$. An analogous statement of relative accuracy holds true for all values of ξ.

We are now in a position to clarify the dimerization ambiguity discussed in Sec. II. Had we derived the continuum approximation using the dual dimerization centered around down triangles would simply amount to the replacement $d\to -d$ in Eqs. (3.12)–(3.14). Therefore the numerical results of Fig. 4 should also be predicted by Eqs. (3.30) and (3.31) applied for $d=-1$ and for some suitable choice of the kink number and polarity which are still free to take the values $\kappa=\pm 1$ and $\nu=\pm 1$ in any combination. It is not difficult to see that Fig. 4 is reproduced very precisely by applying the continuum solution (3.30) and (3.31) for $d=-1$ and $\kappa=1=\nu$. More generally, the mapping of solutions between the two modes of dimerization is given by the simple rule $d\to -d$, $\kappa\to-\kappa$, $\nu\to-\nu$. Therefore the field **n** changes by an overall sign while the corresponding changes in **m** may be inferred also from the general relation (3.12) subjected to the transformation

$$\mathbf{n}\to-\mathbf{n}, \quad \mathbf{d}\to-\mathbf{d}. \tag{3.33}$$

The above rule summarizes the manner in which the continuum model copes with the dimerization ambiguity. In particular, the asymptotic values and the kink (antikink) character of the field **m** are invariant under transformation (3.33) as is evident from Eq. (3.32). Furthermore the continuum model handles quite efficiently questions such as the elusive total moment of a pure AFM wall. Indeed, although the continuum approximation is by construction oblivious to the cutting and pasting of a finite chain, it copes with the various moves described in the concluding paragraphs of Sec. II by mapping solutions of the underlying nonlinear σ model onto other solutions of the same model obtained through the symmetry transformation $\mathbf{n}\to-\mathbf{n}$. Having understood this point, no real ambiguity is present in comparing careful numerical calculations with continuum solutions. Moreover a definition of a magnetization **m** with definite local values is not strictly speaking necessary and is probably unattainable on lattices whose symmetry allows the appearance of parity-breaking gradient terms.[14] This digression is concluded noting that the dimerization process becomes more intricate in higher-dimensional lattices, as discussed in a forthcoming article on the dynamics of topological solitons in 2D antiferromagnets.[15]

We may then return to the standard dimerization scheme of Fig. 1 to which we will consistently adhere in the rest of the paper. An immediate dynamical consequence of the relativistic invariance of Eq. (3.13) at vanishing field and dissipation is that domain walls moving with a constant velocity $v<1(=c)$ can be derived by elementary means. For a freely moving Bloch wall the field **n** is obtained simply by a Lorentz transformation of the static solution (3.30):

$$n_1 = \kappa\tanh u, \quad n_2 = 0, \quad n_3 = \frac{\nu}{\cosh u}, \tag{3.34}$$

where

$$u = \frac{\xi - v\tau}{\sqrt{1-v^2}}. \tag{3.35}$$

The magnetization **m** is then computed from Eq. (3.12) where the first three terms (gradient, dynamical, and DM) are now all important and the fourth term is absent at vanishing field:

$$m_1 = -\frac{\varepsilon}{2\cosh u}\left(\frac{1}{\sqrt{1-v^2}}\frac{\kappa}{\cosh u}+\nu d\right),$$

$$m_2 = -\frac{\varepsilon v}{2\sqrt{1-v^2}}\frac{\kappa\nu}{\cosh u}, \tag{3.36}$$

$$m_3 = \frac{\varepsilon}{2}\tanh u\left(\frac{1}{\sqrt{1-v^2}}\frac{\nu}{\cosh u}+\kappa d\right).$$

In addition to an apparent Lorentz contraction we note that the field **m** develops a nonvanishing component in the second direction due entirely to the wall motion. Incidentally we mention that the continuum approximation breaks down in the ultrarelativistic limit ($v\sim 1$) where the wall width reduces to a few lattice spacings.

This section is completed with a corresponding discussion of *Néel domain walls*. We consider first static solutions for which the vector **n** is confined in the (12) plane and system (3.26) reduces to

$$\Theta = \frac{\pi}{2}, \quad \Phi'' = (d^2+\rho^2)\cos\Phi\sin\Phi. \tag{3.37}$$

Solutions of the second equation are given by

$$\cos\Phi = \kappa\tanh\zeta, \quad \sin\Phi = \frac{\nu}{\cosh\zeta}, \tag{3.38}$$

where the kink number κ and the polarity ν take the same values as those of Eq. (3.29) and ζ is the rescaled spatial coordinate

$$\zeta=\sqrt{d^2+\rho^2}\,\xi. \tag{3.39}$$

The vector **n** reads

$$n_1=\kappa\ \tanh\zeta,\quad n_2=\frac{\nu}{\cosh\zeta},\quad n_3=0, \tag{3.40}$$

and the vector **m** is calculated from Eq. (3.20) to yield

$$m_1=-\frac{\varepsilon}{2}\sqrt{d^2+\rho^2}\,\frac{\kappa}{\cosh^2\zeta},$$

$$m_2=\frac{\varepsilon}{2}\sqrt{d^2+\rho^2}\,\frac{\nu\ \tanh\zeta}{\cosh\zeta},$$

$$m_3=\frac{\varepsilon}{2}\,\kappa d\ \tanh\zeta, \tag{3.41}$$

where we note that all three components are now different from zero.

The numerical calculation of Sec. II did not produce evidence for Néel domain walls because it was based on a relaxation algorithm that inevitably leads to a local minimum of the energy functional. As a result a Néel wall would decay into a topologically equivalent Bloch wall with lower energy. A more precise statement is that (13) walls have lower energy than (12) walls for parameters such that

$$d^2+\rho^2>1\quad\text{or}\quad\left(\frac{D}{J}\right)^2+\frac{g_2}{J}>\frac{g_3}{J}. \tag{3.42}$$

This inequality is certainly satisfied for the uniaxial anisotropy ($g_2=g_3$) used in our numerical calculation and is also typical of orthoferrites. However, at least one example is quoted in the literature, the dysprosium orthoferrite $DyFeO_3$, where the inequality is reversed below 150 K and the role of Bloch and Néel walls is interchanged.[4] Hence, in the bulk of the paper, we shall assume that Eq. (3.42) is satisfied and defer discussion of the consequences of the opposite inequality for the end of the argument. Since Néel walls are unstable one may question whether or not they are relevant for the phenomenology of weak ferromagnets. Actually the inequality (3.42) is marginally satisfied in orthoferrites and Néel walls are substantially stable; they can be experimentally produced and studied apparently without great difficulty. Furthermore they will prove to be crucial in our theoretical analysis of driven domain walls. The situation is different in rhombohedron weak ferromagnets where the two types of walls are separated by a wide energy gap and Néel walls are rather unstable.

We conclude this line of reasoning by quoting an analytical solution for a freely moving Néel wall at vanishing field and dissipation. The field **n** is obtained by a Lorentz transformation of the static solution (3.40),

$$n_1=\kappa\ \tanh w,\quad n_2=\frac{\nu}{\cosh w},\quad n_3=0, \tag{3.43}$$

with

$$w=\sqrt{d^2+\rho^2}\,u=\sqrt{\frac{d^2+\rho^2}{1-v^2}}\,(\xi-v\,\tau), \tag{3.44}$$

whereas the field **m** is calculated from Eq. (3.12) using as input Eq. (3.43) and $h=0$:

$$m_1=-\frac{\varepsilon}{2}\sqrt{\frac{d^2+\rho^2}{1-v^2}}\frac{\kappa}{\cosh^2 w},\quad m_2=\frac{\varepsilon}{2}\sqrt{\frac{d^2+\rho^2}{1-v^2}}\frac{\nu\ \tanh w}{\cosh w}, \tag{3.45}$$

$$m_3=\frac{\varepsilon}{2}\left[\sqrt{\frac{d^2+\rho^2}{1-v^2}}\frac{\kappa\nu v}{\cosh w}+\kappa d\ \tanh w\right].$$

IV. DRIVEN DOMAIN WALLS

The main point of this work is the study of the dynamical response of a domain wall, either Bloch or Néel, to an externally applied magnetic field in the presence of dissipation. During the initial steps of the development it is conceptually simpler to work strictly within the discrete spin model. The continuum description will be invoked at a later stage and will prove more powerful in establishing the complete picture. For definiteness let us assume that the initial configuration is the static Bloch wall calculated in Sec. II for the discrete system (Fig. 3) which is subjected to a uniform field that is turned on at $t=0$ and points in the third direction,

$$\mathbf{h}=(0,0,h)=h\mathbf{e}_3. \tag{4.1}$$

The mathematical problem consists of solving Eq. (3.2) with initial condition supplied by the static wall. One must then study the ensuing evolution and possibly ascertain the formation of a terminal state where the spin configuration moves rigidly with constant velocity v. In particular, one must determine the nature of such a state and the terminal velocity v as functions of the applied field.

To appreciate the results of an explicit numerical solution we first examine the behavior of the spin configuration far from the wall center or, equivalently, determine the fate of the two degenerate ground states after the field is turned on. It is clear that the applied field lifts the degeneracy and creates an imbalance between the two sides of the wall. Actually a field by itself would merely set the ground state in eternal precession. The role of dissipation is also important in that precession eventually dies out and two new static ground-state configurations emerge that are both local minima of the energy functional but now have different energies thanks to the magnetic field. The precise nature of these minima is again determined by optimizing the simplified energy function (2.5) extended to include a Zeeman term:

$$w=(\mathbf{a}\cdot\mathbf{b})+\varepsilon\mathbf{d}\cdot(\mathbf{a}\times\mathbf{b})+\frac{\varepsilon^2}{4}(a_3^2+b_3^2)-\varepsilon h(a_3+b_3). \tag{4.2}$$

Here we have anticipated that the optimal configurations are confined in the (13) plane (hence $a_2=0=b_2$) and have also expressed parameters in their rationalized form.

The original ground state depicted in the first row of Fig. 2 evolves into a state with a field-dependent canting angle δ satisfying the algebraic equation

$$\left(1+\frac{\varepsilon^2}{4}\right)\sin 2\delta-\varepsilon d\cos 2\delta-\varepsilon h\cos\delta=0, \tag{4.3}$$

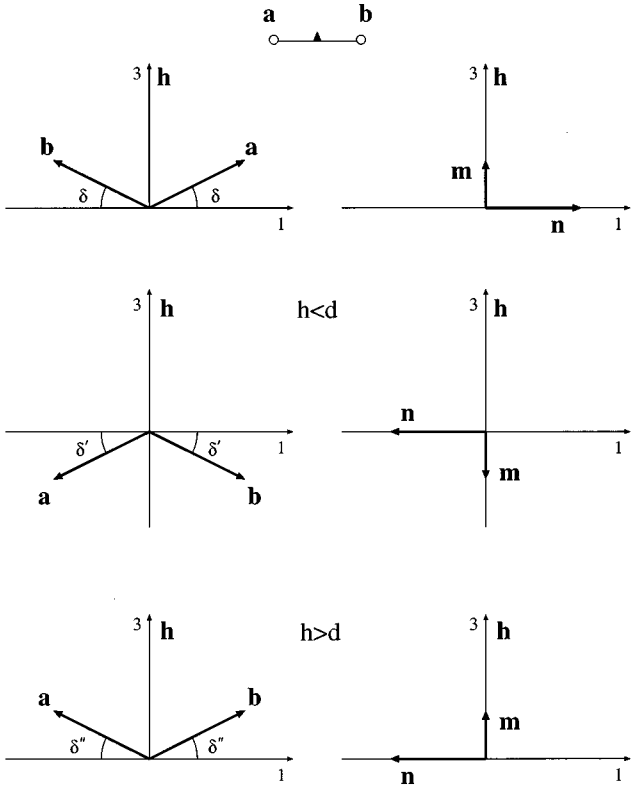

FIG. 5. The fate of the two degenerate ground states of Fig. 2 in the presence of an external field h. Degeneracy is lifted because the second ground state displays a different canting angle ($\delta \neq \delta'$) and higher energy. The third row of the figure illustrates the second ground state in connection with a mild crossover that takes place at $h=d$.

which reduces to Eq. (2.7) at vanishing field ($h=0$). Similarly the ground state shown in the second row of Fig. 2 becomes a state with a different canting angle δ' given by

$$\left(1+\frac{\varepsilon^2}{4}\right)\sin 2\delta' - \varepsilon d \cos 2\delta' + \varepsilon h \cos\delta' = 0. \qquad (4.4)$$

The two states are depicted symbolically in the first and second rows of Fig. 5 and are no longer related by a parity reflection because $\delta \neq \delta'$. A simple numerical solution of the algebraic equations and a corresponding calculation of the energy (4.2) establishes that both states are local minima but the energy of the second solution is higher. The third row in Fig. 5 illustrates the manner in which the second state evolves for a sufficiently strong field ($h>d$). Note that for $h=d$ the solution of Eq. (4.4) is $\delta'=0$. A new element in the region $h>d$ is that the vector **m** points in the same direction (the direction of the magnetic field) for both types of ground states but its magnitude is different in the two cases. The canting angle δ'' is calculated from

$$\left(1+\frac{\varepsilon^2}{4}\right)\sin 2\delta'' + \varepsilon d \cos 2\delta'' - \varepsilon h \cos\delta'' = 0, \qquad (4.5)$$

which is related to Eq. (4.4) by the substitution $\delta' \to -\delta''$. Within the domain of validity of the continuum approximation the various canting angles introduced above can be approximated by

$$\delta \approx \frac{\varepsilon}{2}(d+h), \quad \delta' \approx \frac{\varepsilon}{2}(d-h), \quad \delta'' \approx \frac{\varepsilon}{2}(h-d). \qquad (4.6)$$

This approximation becomes progressively questionable for very strong fields in the region $h \sim 1/\varepsilon$.

Therefore, when the field is turned on, the two ground-state configurations (domains) on the two sides of the domain wall are expected to adjust to those of Fig. 5 at some characteristic time interval τ_0. During the transient period, $\tau \lesssim \tau_0$, precession effects are strong and the wall behaves in a complicated manner. However, for $\tau > \tau_0$, the two sides have adjusted to the new static domains one of which has higher energy density. We thus expect the whole spin configuration to reach a terminal state where the domain with the lower energy expands perpetually at the expense of the other; whence the motion of the domain wall with a constant terminal velocity $v=v(h)$.

The qualitative picture described above can be confirmed by a straightforward numerical calculation in the discrete spin model. We solve the initial-value problem for Eq. (3.2) for our standard choice of parameters ($\varepsilon=10^{-2}$, $\rho=1=d$) together with a typical dissipation constant $s\gamma=10^{-2}$ or $\lambda=2$. Simulations were performed for a number of values of the rationalized field h, using as an initial condition the static Bloch wall calculated numerically in Sec. II at vanishing field.

Explicit results for $h=1/2$ are given in Figs. 6 and 7. The wall motion was monitored by tracking the point where the first component of **n** vanishes, using linear interpolation to locate its actual position between two lattice sites. The corresponding velocity is plotted in Fig. 6(a) and displays a transient period after which it quickly approaches a terminal value $v=0.214$ that should be accurate to all three significant figures. Figure 6(b) illustrates the time evolution of the ground-state configurations away from the wall center concentrating on the third component of **m** whose initial ($\tau=0$) asymptotic ($\xi=\pm\infty$) values are those of Eq. (2.9). After the same transient period m_3 approaches the terminal value $m_3=\sin\delta=0.007\,499\,39$ far to the left of the wall and the value $m_3=-\sin\delta'=-0.002\,501\,08$ far to the right, which are in excellent agreement with the accurate roots of the algebraic equations (4.3) and (4.4) and in good agreement with the approximate roots (4.6). Finally Fig. 7 displays the terminal state of the wall with numerical data for the spin presented using the technique discussed in Sec. II in connection with Fig. 3.

A simple comparison of Figs. 3 and 7 reveals that the terminal state has acquired a significant Néel component ($n_2 \neq 0$) and is thus appreciably different from the original Bloch wall. In particular, the terminal state of the driven Bloch wall has no resemblance to the freely moving Bloch wall of Eqs. (3.34)–(3.36). To push this picture further we repeated the calculation for a stronger field ($h=3/2$) which was expected to lead to a stronger Bloch-Néel hybridization. The results of Fig. 8 came as a surprise in that the original Bloch wall ($n_2=0$) had turned completely into a Néel wall ($n_3=0$). Incidentally we note that we are now in the field regime $h>d$, because $h=3/2$ and $d=1$, where the vector **m** points in the field direction on both sides, as was anticipated by the discussion of Fig. 5 and is evident in Fig. 8(b). How-

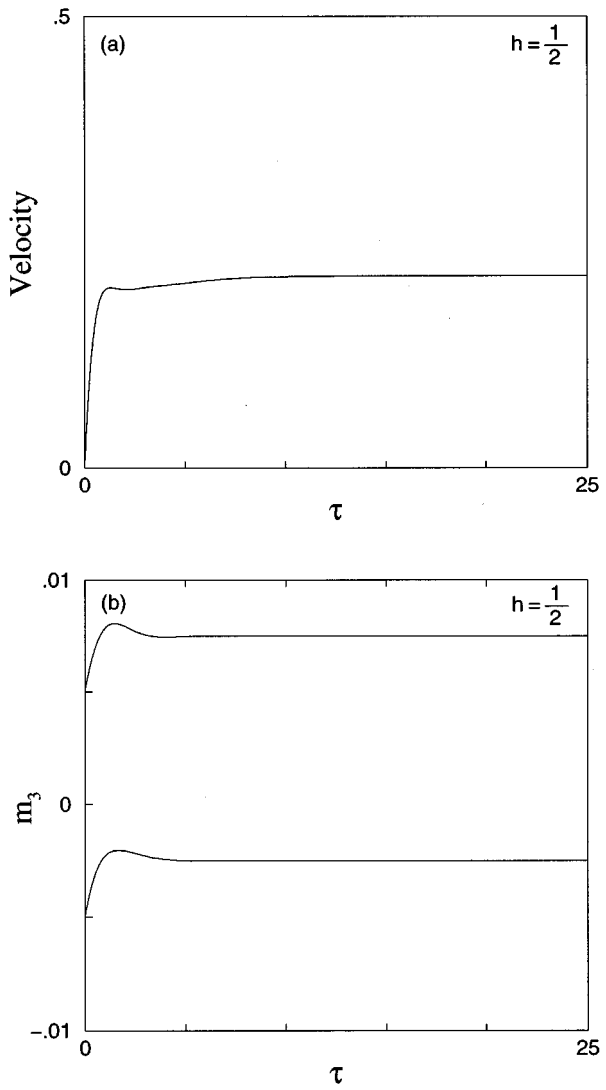

FIG. 6. Dynamical response of the static Bloch wall of Fig. 3 to an applied field $h=1/2$, calculated numerically within the discrete spin model. (a) The wall velocity approaches a terminal value $v=0.214$ after a transient period $\tau_0 \approx 5$. (b) Response of the ground state monitored by the values of m_3 far to the left of the wall (upper curve) and far to its right (lower curve). The corresponding terminal values are given in the text.

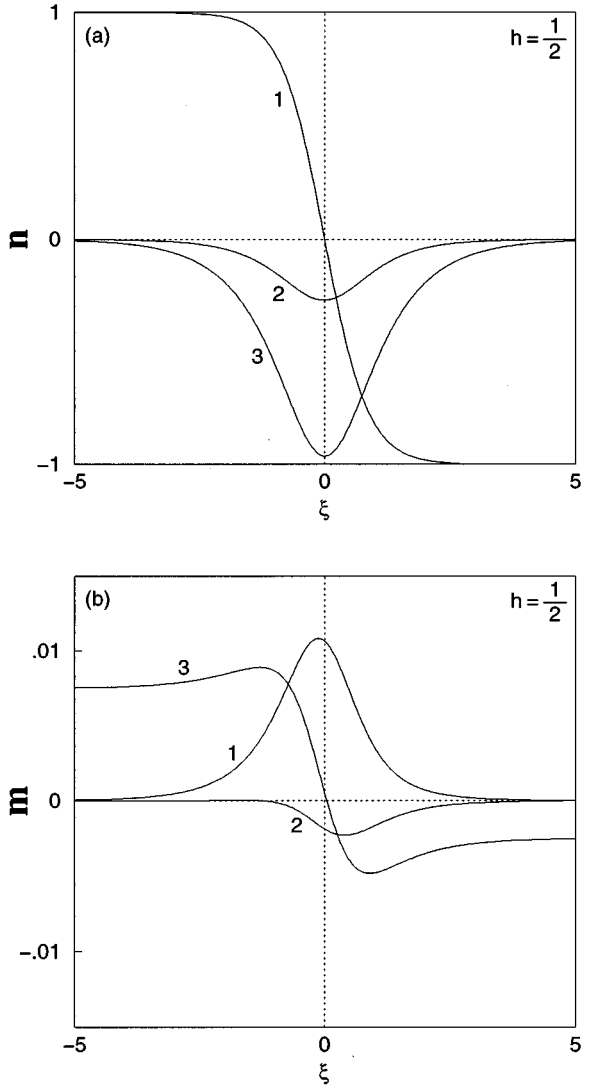

FIG. 7. The terminal state of the Bloch wall of Fig. 3 driven by a field $h=1/2$, calculated numerically within the discrete spin model. Note a significant Bloch-Néel hybridization ($n_2 \neq 0$).

ever the mild crossover at $h=d$ is not the important issue in Fig. 8. Rather this calculation suggests the existence of a genuine critical field h_c above which a driven Bloch wall is always converted into a Néel wall. The critical field h_c need not coincide with the crossover value $h=d$.

A detailed investigation of this important issue based only on numerical simulations would be tedious. Hence we recall at this point the continuum model which will prove to be a very powerful tool. For instance, the continuum model may be used to provide a simple explanation for the existence of a critical field which will also yield a rough estimate of its actual value. The important issue is again inequality (3.42) that governs the relative stability of Bloch and Néel walls. Suppose that Eq. (3.42) is indeed satisfied and thus Néel or (12) walls are relatively unstable to Bloch or (13) walls. A simple inspection of Eq. (3.14) applied for $\mathbf{d}=d\mathbf{e}_2$ and $\mathbf{h}=h\mathbf{e}_3$ suggests that the presence of an applied field may change the situation because the effective anisotropies along the second and third axes now appear with coefficients $d^2+\rho^2$ and $1+h^2$. At low fields, where the inequality $d^2+\rho^2>1+h^2$ is still satisfied, (13) walls continue to be stable but may develop a small (12) component due to the applied field. However, at a sufficiently strong field where the inequality is reversed, (13) walls become relatively unstable to (12) walls and a complete dynamical conversion takes place in the terminal state. The critical field is then estimated from $d^2+\rho^2 \sim 1+h^2$ or

$$h_c \sim \sqrt{d^2+\rho^2-1}, \tag{4.7}$$

in units specified by Eq. (3.4), and is clearly not related to the crossover value $h=d$ discussed in connection with Fig. 5. Now, applied for $d=1=\rho$, the above estimate yields $h_c \sim 1$ which explains the Bloch-Néel hybridization observed in Fig. 7 for $h=1/2$ as well as the complete dynamical conversion of a driven Bloch wall at $h=3/2$ shown in Fig. 8. The picture is completed in three steps described in the following three subsections.

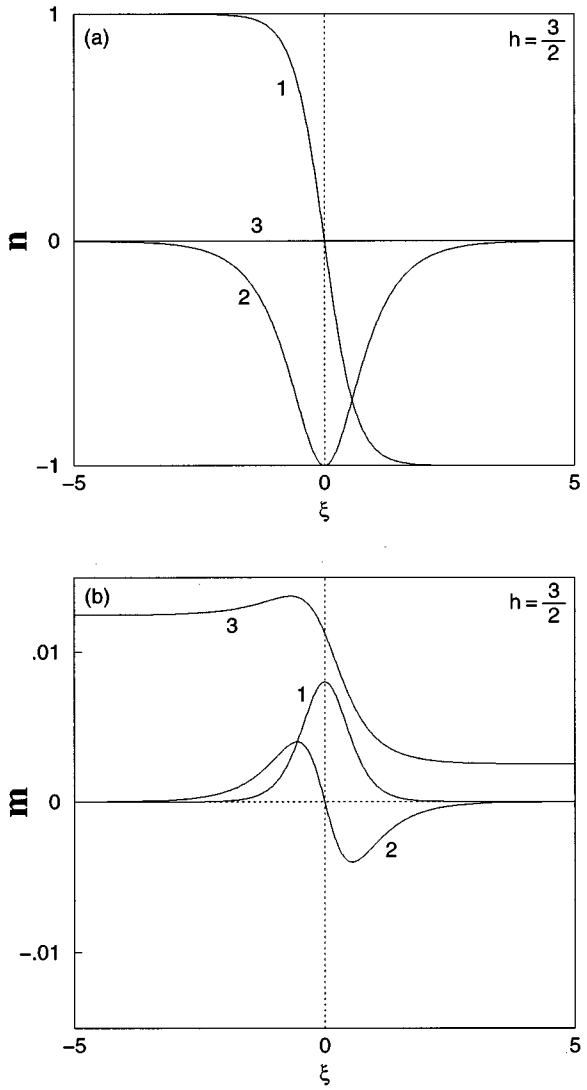

FIG. 8. The terminal state of the Bloch wall of Fig. 3 driven by a field $h=3/2$, calculated numerically within the discrete spin model. This state is very accurately reproduced by the continuum solution for a driven Néel wall given by Eqs. (4.43) and (4.44) and indicates a complete dynamical conversion of the initial Bloch wall.

A. Virial theorem and mobility

A driven domain wall that has reached a terminal state with constant velocity v is described by a field $\mathbf{n}$ of the form

$$\mathbf{n}=\mathbf{n}(\xi-v\tau). \tag{4.8}$$

Time derivatives may then be replaced by $\dot{\mathbf{n}}=-v\mathbf{n}'$ where the prime denotes differentiation with respect to either ξ or the entire argument $\xi-v\tau$. This distinction will not be made explicit in the following but one must remember that the argument of all fields is $\xi-v\tau$. Equation (3.13) becomes

$$\lambda v(\mathbf{n}\times\mathbf{n}')=\mathbf{n}\times\mathbf{f}, \tag{4.9}$$

where the effective field $\mathbf{f}$ takes the reduced form

$$\mathbf{f}=-(1-v^2)\mathbf{n}''-2v(\mathbf{h}\times\mathbf{n}')+(\mathbf{h}\times\mathbf{d}) +(\mathbf{n}\cdot\mathbf{h})\mathbf{h}+(\mathbf{n}\cdot\mathbf{d})\mathbf{d}+\rho^2 n_2\mathbf{e}_2+n_3\mathbf{e}_3 \tag{4.10}$$

and the problem is accordingly reduced to the solution of ordinary differential equations. In this subsection we shall not attempt to find explicit solutions of the above equations. Instead we will derive a general virial relation that can be used for a direct calculation of the mobility. The method is an elementary adaptation of related work in the theory of magnetic bubbles.[16]

An equivalent form of Eq. (4.9) is obtained by taking the cross product of both sides with $\mathbf{n}$ and using the constraint $\mathbf{n}^2=1$:

$$\lambda v\mathbf{n}'=\mathbf{f}-(\mathbf{f}\cdot\mathbf{n})\mathbf{n}. \tag{4.11}$$

Next we contract both sides with the vector $\mathbf{n}'$ and use the identity $(\mathbf{n}\cdot\mathbf{n}')=0$ which is also a consequence of the constraint:

$$\lambda v\mathbf{n}'^2=(\mathbf{f}\cdot\mathbf{n}'). \tag{4.12}$$

The right-hand side of Eq. (4.12) may be written as

$$(\mathbf{f}\cdot\mathbf{n}')=\sigma', \tag{4.13}$$

which is indeed an identity if $\mathbf{f}$ is taken from Eq. (4.10) and σ is given by

$$\sigma=\frac{1}{2}[-(1-v^2)\mathbf{n}'^2+2(\mathbf{h}\times\mathbf{d})\cdot\mathbf{n} +(\mathbf{n}\cdot\mathbf{h})^2+(\mathbf{n}\cdot\mathbf{d})^2+\rho^2 n_2^2+n_3^2]. \tag{4.14}$$

Equation (4.12) is then written as

$$\lambda v\mathbf{n}'^2=\sigma', \tag{4.15}$$

whose advantage is that the right-hand side is a total derivative.

The virial theorem is obtained simply by integrating both sides of Eq. (4.15) over all space,

$$\lambda v\int\mathbf{n}'^2 d\xi=\sigma(\infty)-\sigma(-\infty), \tag{4.16}$$

where $\sigma(\pm\infty)$ are the boundary values of σ. Inspection of Eq. (4.14) taking into account that $\mathbf{d}=d\mathbf{e}_2$ and $\mathbf{h}=h\mathbf{e}_3$, together with the fact that only the first component of $\mathbf{n}$ survives at large distances, yields

$$\lambda v\int\mathbf{n}'^2 d\xi=-hd[n_1(\infty)-n_1(-\infty)]. \tag{4.17}$$

One may also recall the kink number introduced in Sec. II,

$$\kappa=\frac{1}{2}[n_1(\infty)-n_1(-\infty)], \tag{4.18}$$

to write the virial relation in the final form

$$\lambda v\int_{-\infty}^{\infty}\mathbf{n}'^2 d\xi=-2\kappa dh. \tag{4.19}$$

It is important to note that the only contribution on the right-hand side of this relation originates in the crossed $(\mathbf{h}\times\mathbf{d})$ term discussed earlier, which now proves to be crucial for the very existence of driven domain walls in a terminal state; for, otherwise, the right-hand side of Eq. (4.19) would vanish leading to an obvious contradiction. Therefore, if the La-

grangian of Eq. (2.30) in Ref. 4 is taken at face value, driven domain walls in a terminal state would not exist for an antisymmetric DM interaction. Relation (4.19) also contradicts the existence of static ($v=0$) walls in the presence of an applied field ($h\neq 0$) as well as the existence of a rigidly moving wall ($v\neq 0$) at vanishing dissipation ($\lambda=0$) and a nonvanishing field ($h\neq 0$).

Virial relation (4.19) will be used in two ways. First, as a check of consistency of both numerical and analytical results. For example, the numerical calculation presented in Figs. 6 and 7 must be consistent with Eq. (4.19). Indeed using the input parameters $\lambda=2$, $d=1$, $\kappa=-1$, and $h=1/2$, the calculated terminal velocity $v=0.214$ of Fig. 6(a) and the field **n** of Fig. 7(a) to compute the integral in Eq. (4.19) numerically, the virial relation is satisfied to at least three significant figures.

A second more tangible application of the virial theorem is an exact calculation of the wall mobility. Equation (4.19) is consistent with a *linear* mobility relation at *low fields* where

$$v\approx\mu h,\quad \frac{1}{\mu}=-\frac{\lambda}{2\kappa d}\int_{-\infty}^{\infty}\mathbf{n}'^{2}d\xi, \tag{4.20}$$

supplemented by the stipulation that the integral be evaluated using as input the profile of the initial *static* domain wall, as is appropriate in the limit of the vanishing field where the velocity also vanishes. The sign of the mobility μ is not definite because Eq. (4.20) yields information on both the direction and the magnitude of the wall velocity. One should add that the above result is insensitive to the dimerization ambiguity discussed earlier because Eq. (4.19) is invariant under transformation (3.33).

We must now distinguish two cases depending on whether the initial wall is Bloch or Néel. For a Bloch wall we may use the static solution (3.30) in Eq. (4.20) to obtain

$$v\approx\mu_1 h,\quad \mu_1=-\frac{\kappa d}{\lambda}, \tag{4.21}$$

whereas the Néel mobility is calculated from Eqs (3.40) and (4.20):

$$v\approx\mu_2 h,\quad \mu_2=-\frac{\kappa}{\lambda}\frac{d}{\sqrt{d^2+\rho^2}}. \tag{4.22}$$

We also consider the dimensionless ratio

$$\frac{\mu_1}{\mu_2}=\sqrt{d^2+\rho^2} \tag{4.23}$$

and relate it to the inequality (3.42) discussed in connection with the potential instability of Néel walls. When this inequality is satisfied Néel walls are relatively unstable to Bloch walls and their mobility is smaller ($\mu_1>\mu_2$). The measured[17,18] mobility ratio in $YFeO_3$ is $\mu_1/\mu_2=1.06$. In $DyFeO_3$ below 150 K, the inequality (3.42) is reversed, (13) walls become unstable, and their mobility is predicted to be smaller than the mobility of (12) walls ($\mu_1<\mu_2$).

One can also relate the mobility ratio to the experimentally observed magnon activation frequencies in the absence of the external field. The simplest way to calculate the frequencies is to consider the Lagrangian (3.17) at vanishing field ($h=0$) expressed in terms of the spherical variables (3.24):

$$L=\frac{1}{2}[(\dot\Theta^2+\sin^2\Theta\dot\Phi^2)-(\Theta'^2+\sin^2\Theta\Phi'^2)$$
$$-(d^2+\rho^2)\sin^2\Theta\ \sin^2\Phi-\cos^2\Theta]. \tag{4.24}$$

Small fluctuations around the ground state $\Theta=\pi/2$ and $\Phi=0$ or π are calculated by inserting $\Theta=\pi/2+\theta$ and $\Phi=\phi$ or $\pi+\phi$ in Eq. (4.24) and keeping terms that are at most quadratic in θ and ϕ. The resulting quadratic Lagrangian

$$L\approx\frac{1}{2}[\dot\theta^2-\theta'^2-\theta^2]+\frac{1}{2}[\dot\phi^2-\phi'^2-(d^2+\rho^2)\phi^2] \tag{4.25}$$

describes two uncoupled free fields with dispersions

$$\Omega_1(k)=\sqrt{\omega_1^2+k^2},\quad \Omega_2(k)=\sqrt{\omega_2^2+k^2}, \tag{4.26}$$

where ω_1 and ω_2 are the magnon activation frequencies

$$\omega_1=1,\quad \omega_2=\sqrt{d^2+\rho^2}, \tag{4.27}$$

expressed in the rationalized units employed throughout this paper.

For the moment we consider the dimensionless ratio ω_2/ω_1 and compare it to the right-hand side of Eq. (4.23) to obtain the parameter-free theoretical prediction

$$\frac{\mu_1}{\mu_2}=\frac{\omega_2}{\omega_1}. \tag{4.28}$$

On the other hand, Ref. 10 gives the values $\omega_1=11\ \mathrm{cm}^{-1}$ and $\omega_2=17\ \mathrm{cm}^{-1}$ (or $\omega_2/\omega_1=1.55$) for the frequencies actually observed in $YFeO_3$, while Ref. 4 adopts values in the range $\omega_1=(11-13)\ \mathrm{cm}^{-1}$ and $\omega_2=(15-20)\ \mathrm{cm}^{-1}$ (or $1.15<\omega_2/\omega_1<1.82$). These values are not terribly inconsistent with the measured mobility ratio $\mu_1/\mu_2=1.06$, in view of the simplicity of the classical spin model and the fact that anharmonic corrections to the calculated frequencies (4.27) have been neglected.

This subsection is concluded by translating some of the quantities calculated above in ordinary units. The definition of the dimensionless time variable τ in Eq. (3.10) implies that the magnon activation frequencies of Eq. (4.27) are measured in units of $2\varepsilon sJ$. Hence

$$\omega_1=2sJ\sqrt{\frac{g_3}{J}},\quad \omega_2=2sJ\sqrt{\left(\frac{D}{J}\right)^2+\frac{g_2}{J}}. \tag{4.29}$$

These results could also be derived by calculating the magnon spectrum of the 1D discrete spin model of Sec. II using standard spin-wave techniques. The corresponding frequencies in the 3D model were calculated in Refs. 10 and 19 within the harmonic approximation and read in current notation

$$\omega_1=2sJ\sqrt{\frac{zg_3}{2J}},\quad \omega_2=2sJ\sqrt{\frac{z}{2}}\ \sqrt{\frac{z}{2}\left(\frac{D}{J}\right)^2+\frac{g_2}{J}}, \tag{4.30}$$

where $z=6$ is the coordination number of the 3D lattice, while setting $z=2$ reproduces the 1D results of Eq. (4.29). These are further examples of correspondence between the microscopic parameters of the 1D and 3D models; see Eq. (3.19). We also take this opportunity to mention that the positivity condition on g_2 may be relaxed to some extent, as long as the arguments in the square roots of Eqs. (4.29) and (4.30) remain positive.

Finally we translate the mobilities (4.21) and (4.22) in ordinary units recalling that velocity is measured in units of the limiting velocity c of Eq. (3.18). Then

$$\mu_1=-\frac{\kappa c}{2s\gamma}\frac{g_0\mu_0}{2sJ}\frac{D}{J}\left[\frac{g_3}{J}\right]^{-1/2},$$

$$\mu_2=-\frac{\kappa c}{2s\gamma}\frac{g_0\mu_0}{2sJ}\frac{D}{J}\left[\left(\frac{D}{J}\right)^2+\frac{g_2}{J}\right]^{-1/2}. \tag{4.31}$$

We shall not attempt to generalize the above formulas to an arbitrary coordination number except to state that the parameter-free prediction (4.28) remains true in any dimension.

Perhaps the earliest theoretical calculation of the $v(h)$ curves is that of Gyorgy and Hagedorn[20] who arrived at two formulas of type (1.1), one for each kind of wall. This early attempt suffers from two drawbacks. First, the calculated mobilities appear to be proportional to the exchange rather than the DM constant, which is obviously false on physical grounds because the driving issue is the DM interaction. Second, as we shall see shortly, a description in terms of two completely independent $v(h)$ curves is also false. The situation was improved in more recent publications[21,22] but several issues remained unclear.

B. Analytical solution for Néel walls

One must now consider the case of a field of arbitrary strength and possibly make contact with the semiempirical relation (1.1). Although the numerical simulation is still an option, one might also hope to derive analytical solutions within the continuum model. Such a hope is partially fulfilled in the present subsection.

Thus we return to Eq. (4.11) where the effective field **f** of Eq. (4.10) is again derived from a variational argument of the form (3.22) by generalizing the energy functional $\mathcal{F}$ of Eq. (3.23) to

$$\mathcal{F}=\frac{1}{2}\int[(1-v^2)\mathbf{n}'^2+2v\mathbf{h}\cdot(\mathbf{n}\times\mathbf{n}')+2(\mathbf{h}\times\mathbf{d})\cdot\mathbf{n}+(\mathbf{n}\cdot\mathbf{h})^2+(\mathbf{n}\cdot\mathbf{d})^2+\rho^2n_2^2+n_3^2]d\xi. \tag{4.32}$$

Expressed in terms of the spherical variables the above functional reads

$$\mathcal{F}=\frac{1}{2}\int[(1-v^2)(\Theta'^2+\sin^2\Theta\Phi'^2)+2vh\ \sin^2\Theta\Phi'-2hd\ \sin\Theta\ \cos\Phi+(d^2+\rho^2)\sin^2\Theta\ \sin^2\Phi+(1+h^2)\cos^2\Theta]d\xi. \tag{4.33}$$

One may now use the general form of the effective field **f** from Eq. (3.22) in Eq. (4.11) and a repeated application of the chain rule to derive the two independent equations

$$\lambda v\Theta'=\frac{\delta\mathcal{F}}{\delta\Theta},\quad \lambda v\ \sin^2\Theta\Phi'=\frac{\delta\mathcal{F}}{\delta\Phi}, \tag{4.34}$$

whose explicit forms read

$$\lambda v\Theta'=-(1-v^2)\Theta''-hd\ \cos\Theta\cos\Phi+[(1-v^2)\Phi'^2+2vh\Phi'+(d^2+\rho^2)\sin^2\Phi-1-h^2]\cos\Theta\sin\Theta \tag{4.35}$$

and

$$\lambda v\ \sin^2\Theta\Phi'=-(1-v^2)(\sin^2\Theta\Phi')'-vh(\sin^2\Theta)'+hd\sin\Theta\ \sin\Phi+(d^2+\rho^2)\times\sin^2\Theta\cos\Phi\sin\Phi. \tag{4.36}$$

This is a rather complicated system of nonlinear differential equations and its analytical solution appears to be hopeless.

Nevertheless the system simplifies enormously when we restrict attention to strictly Néel walls, i.e.,

$$\Theta=\frac{\pi}{2}, \tag{4.37}$$

for which the first equation is trivially satisfied and the second reduces to

$$-(1-v^2)\Phi''+(d^2+\rho^2)\cos\Phi\sin\Phi=\lambda v\Phi'-hd\ \sin\Phi. \tag{4.38}$$

We now attempt to solve simultaneously the two equations

$$(1-v^2)\Phi''=(d^2+\rho^2)\cos\Phi\sin\Phi,\qquad \lambda v\Phi'=hd\ \sin\Phi, \tag{4.39}$$

in the sense that every solution of Eqs. (4.39) will be a solution of Eq. (4.38). The first equation gives

$$\cos\Phi=\kappa\ \tanh w,\quad \sin\Phi=\frac{\nu}{\cosh w}, \tag{4.40}$$

where κ and ν are the kink number and polarity discussed in Sec. III and w is the argument of Eq. (3.44). The important observation is that the angle Φ of Eq. (4.40) also satisfies the second equation in Eq. (4.39) provided that the parameters are related by

$$\frac{v}{\sqrt{1-v^2}}=\mu_2 h, \tag{4.41}$$

where μ_2 is precisely the mobility of a Néel wall calculated previously in Eq. (4.22). The relativisticlike relation (4.41) may then be written as

$$v=\frac{\mu_2 h}{\sqrt{1+(\mu_2 h)^2}} \tag{4.42}$$

and thus reproduces Eq. (1.1) applied with a mobility $\mu=\mu_2$ appropriate for a Néel wall. The lack of a limiting

velocity c in Eq. (4.42) is, of course, due to the current use of rationalized physical units where the limiting velocity is equal to one.

To complete the solution we calculate the field **n**, from Eqs. (4.37) and (4.40),

$$n_1=\kappa\ \tanh w,\quad n_2=\frac{\nu}{\cosh w},\quad n_3=0, \tag{4.43}$$

and the field **m** from the general relation (3.12):

$$m_1=-\frac{\varepsilon}{2}\sqrt{\frac{d^2+\rho^2}{1-v^2}}\frac{\kappa}{\cosh^2 w},$$

$$m_2=\frac{\varepsilon}{2}\sqrt{\frac{d^2+\rho^2}{1-v^2}}\frac{\nu\ \tanh w}{\cosh w},$$

$$m_3=\frac{\varepsilon}{2}\left[\sqrt{\frac{d^2+\rho^2}{1-v^2}}\frac{\kappa\nu v}{\cosh w}+\kappa d\ \tanh w+h\right]. \tag{4.44}$$

A notable feature of this result is that a driven Néel wall differs from the freely moving Néel wall of Eq. (3.45) only by an additive field dependent constant in m_3 and the fact that the velocity is now a definite function of the applied field given by Eq. (4.42). As a check of consistency one can verify explicitly that the above solution satisfies the virial relation (4.19).

The seeds for the analytical solution presented in this subsection may be found in the paper of Zvezdin[21] but its precise form and physical content remained unclear. In particular, no distinction was made between Bloch and Néel walls. Nevertheless the above work also contains the seeds for the crossed term $(\mathbf{h}\times\mathbf{d})$ discussed earlier in the present paper. But the formalism of Ref. 21 is unwieldy and was clearly not adopted in more recent publications.[4]

C. Dynamical conversion of Bloch walls

We now resume the study of driven Bloch walls initiated by the numerical simulation presented in the beginning of the main section. It would be natural to expect that the corresponding $v(h)$ curve is analogous to Eq. (4.42), namely,

$$v=\frac{\mu_1 h}{\sqrt{1+(\mu_1 h)^2}}\qquad \text{(false)}, \tag{4.45}$$

where μ_1 is now the Bloch mobility of Eq. (4.21). In fact, this appears to be the implicit assumption made in all earlier treatments.[4] However, the numerical results presented in Figs. 6, 7, and 8 already disprove such an assumption.

For example, the accurate terminal velocity $v=0.214$ calculated numerically for $h=1/2$ [see Fig. 6(a)] clearly disagrees with the value $v=0.224$ obtained from Eq. (4.45) applied with $\mu_1=1/2$; here the Bloch mobility μ_1 was calculated from Eq. (4.21) for our standard choice of parameters $d=1=\rho$, $\lambda=2$, and $\kappa=-1$. A more impressive statement can be made at $h=3/2$ where the numerically calculated terminal velocity ($v=0.468$) again disagrees with Eq. (4.45) but is, instead, very accurately predicted by Eq. (4.42) applied with a *Néel mobility* $\mu_2=1/2\sqrt{2}$ given by Eq. (4.22). This is a concrete confirmation of our earlier statement that a critical field h_c exists above which a driven Bloch wall is converted completely into a Néel wall. A definitive confirmation is achieved by noting that the numerically calculated detailed profile of a driven Bloch wall given in Fig. 8 for $h=3/2$ is reproduced very precisely by the analytical solution for a driven Néel wall given in Eqs. (4.43) and (4.44).

Yet the results for $h=1/2$ presented in Figs. 6 and 7 indicate that there exists a field regime ($h<h_c$) where the terminal state of a driven Bloch wall is hybridized and the velocity is not predicted by either Eq. (4.42) or (4.45); except for very low fields where $v\approx\mu_1 h$, in accord with our results in subsection A. In other words, the mobility curves for the two types of domain walls coincide for $h>h_c$ and are both given by the relativistic formula (4.42) applied with a Néel mobility μ_2. Below h_c a bifurcation takes place whereby the two curves split and eventually reach the (low-field) linear regime at different slopes; $v\approx\mu_1 h$ and $v\approx\mu_2 h$ for Bloch and Néel walls, respectively. Although we have been unable to obtain an analytical solution of Eqs. (4.35) and (4.36) for driven Bloch walls in the region $h<h_c$, the bifurcation described above was unambiguously established by repeating the numerical calculation for a number of field values in the range $0<h<3/2$. The results are summarized in Fig. 9 which is more or less self-explanatory.

Our inability to obtain a complete analytical solution is due to the nontrivial Bloch-Néel hybridization that takes place in the region $h<h_c$ (see Fig. 7). A related technical reason is that the contribution of the nonrelativistic term $2(\mathbf{h}\times\dot{\mathbf{n}})$ is now crucial, while it had droped out of Eq. (4.38) describing driven Néel walls. The same fact explains the relativistic nature of the Néel mobility formula (4.42) and is the reason why the corresponding expression for Bloch walls given by Eq. (4.45) is false. At any rate, the picture obtained by the combination of analytical and numerical results derived so far is essentially complete and we now turn to the discussion of its implications.

First we return to the rough estimate of the critical field given by Eq. (4.7) which yields $h_c\sim 1$ for our standard choice of parameters, while the numerical results of Fig. 9 indicate a value $h_c\approx 0.8$. Such a discrepancy is not surprising because the argument leading to Eq. (4.7) ignores more subtle effects from the remaining terms in Eq. (3.14). As a consequence, Eq. (4.7) is, at best, a rough overestimate of the true critical field. Nevertheless Eq. (4.7) provides a useful guide especially when it is expressed in terms of the mobility ratio (4.23) to yield

$$h_c\sim\sqrt{(\mu_1/\mu_2)^2-1}. \tag{4.46}$$

In a typical orthoferrite such as $YFeO_3$ inequality (3.42) is satisfied as evidenced by the measured mobility ratio $\mu_1/\mu_2=1.06$. Therefore, two distinct mobility curves ($v\approx\mu_1 h$ and $v\approx\mu_2 h$) emanate from the low-field region that must join up at a critical value of the driving field and thereafter follow a single curve given by the relativistic Néel formula (4.42). In view of the small mobility ratio the bifurcation region is expected to be narrow and may easily have been missed in the analysis of existing experimental data, especially because other complications are present such as magnetoelastic anomalies.[4] However our detailed theoretical results for both the mobility curves and the profiles of driven domain walls may help to reassess the experimental situation.

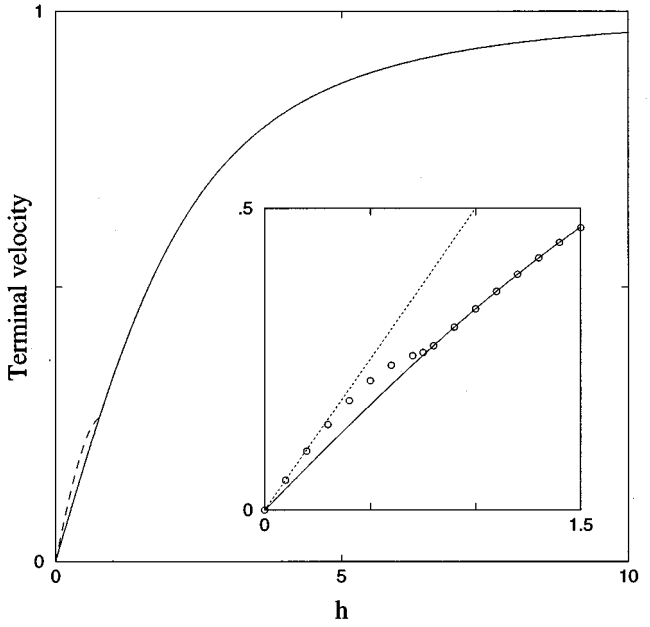

FIG. 9. Mobility curves for driven Bloch and Néel walls. The Néel curve (solid line) is given by the analytical expression (4.42) applied with a mobility μ_2 calculated from Eq. (4.22); $\mu_2=1/2\sqrt{2}$ for our standard choice of parameters $\kappa=-1$, $d=1=\rho$, and $\lambda=2$. The Bloch curve (dashed line) was obtained by a numerical simulation in the discrete spin model and takes off with a slope μ_1 at low fields ($v\approx\mu_1 h$) where $\mu_1=1/2$ is the Bloch mobility calculated from Eq. (4.21). The two curves join up at a critical field $h_c\approx 0.8$ and thereafter both follow the analytical Néel result of Eq. (4.42). The inset demonstrates the bifurcation regime in greater detail, with numerical data for the Bloch curve represented by open circles and a dotted straight line indicating the initial slope $\mu_1=1/2$.

When inequality (3.42) is saturated the critical field vanishes and the bifurcation region shrinks to zero. Putting it differently, the terminal state is always a (12) wall and the mobility curve is that of Eq. (4.42) irrespective of the nature of the initial state. This simplified picture remains *a fortiori* correct when inequality (3.42) is reversed and may describe the dynamics of domain walls in $DyFeO_3$ below 150 K.

In contrast, the observed great disparity between Bloch and Néel walls in rhombohedron weak ferromagnets should be expected to enhance the bifurcation regime and make it a dominant feature in the analog of Fig. 9. As a consequence, the mobility curve for Bloch walls will depart significantly from the relativistic result of Eq. (1.1) for most field values of practical interest. Of course, a detailed calculation in this case will require a modification of the Hamiltonian to include a sixth-order single-ion anisotropy in the basal plane and possibly alternative forms of the dissipative term.[4]

We also comment on the domain of validity of the continuum model in the presence of an applied field. The condition $\varepsilon h \ll 1$ of Eq. (3.5) is well satisfied in Fig. 9 where the maximum displayed value is $h=10$ for which $\varepsilon h=0.1$. For greater field values the continuum approximation begins to deteriorate and eventually breaks down when $\varepsilon h\sim 1$. Another way for stating the same fact is that the wall velocity approaches the relativistic limiting velocity c and the wall width reduces to a few lattice spacings. Under such extreme conditions one must again resort to the discrete spin model of Sec. II. However a new element arises when Fig. 5 is pushed to extreme field values. The second ground state, now described by the third row of Fig. 5, ceases to be a local minimum and becomes a saddle point of the energy (4.2) at a new critical field $h_c'\sim f(d)/\varepsilon$ where $f(d)$ is some function of d that can be determined numerically. In our standard numerical example $h_c'\approx 190$. Therefore, when a field with strength above h_c' is turned on, the imbalance between the two sides of the wall becomes catastrophic and the motion looks more like an avalanche rather than a steady terminal state. In this respect, the field h_c' may be interpreted as the analog of the critical Walker field in ordinary ferromagnets and seems to be the main preoccupation of Ref. 21. Nonetheless such a field regime does not appear to be of great practical value because the corresponding wall velocities have practically reached the limiting velocity c.

Finally, we mention that the general subject of dynamical conversion of domain walls was discussed previously in different physical contexts. For instance, mutual conversion of xy and yz kinks was studied in Ref. 23 for an easy-plane antiferromagnetic chain immersed in an in-plane magnetic field. Although the above work addresses the question of freely moving (instead of driven) kinks in the absence of dissipation, a field-dependent critical velocity was found after which dynamical conversion takes place. The closest example to our current work is discussed in Ref. 24 which considers the effect of a small ''symmetric'' correction to the antisymmetric DM interaction. Freely moving domain walls in the absence of both dissipation and an applied field were then shown to undergo dynamical conversion at some critical velocity. On the other hand, we have established that *driven* Bloch walls in the presence of dissipation are dynamically converted for $h>h_c$ even in the absence of a ''symmetric'' DM interaction; including the latter in our model will only lead to a compounded effect. Therefore the results of Ref. 24 need to be reanalyzed in the light of our current conclusions.

V. CONCLUDING REMARKS

We believe to have presented a complete study of the domain-wall dynamics within the limits of the simplest nontrivial model of a weak ferromagnet which may serve as a prototype for more realistic calculations. From a purely theoretical point of view the new elements that are likely to survive the specific model are (a) a clear analysis of the dimerization ambiguity inherent in all physical systems involving antiferromagnetic interactions, (b) a related derivation of a parity-breaking gradient term in the magnetization **m**, and (c) the identification of a crossed ($\mathbf{h}\times\mathbf{d}$) term in the nonlinear σ model that governs the dynamics of the field **n**. These elements are important for a correct understanding of both structural and dynamical properties of WFM domain walls and were for the most part absent in earlier treatments.[4]

At a more practical level we have presented a complete calculation of driven domain walls whose main features are (a) a virial theorem that underlies the existence of a terminal state and allows a simple calculation of the low-field mobilities, (b) a critical field h_c above which Bloch walls are dy-

namically converted into Néel walls, and (c) a related bifurcation process that leads to a new and interesting picture of the mobility curves. These features should be present also in realistic weak ferromagnets and could be established experimentally.

A closer look at orthoferrites should entail a more detailed justification of our main results within the proper 3D crystal environment. Such a study would remove some uncertainty concerning the correspondence between microscopic parameters and those appearing in the continuum model. Incidentally the original determination of parameters carried out by Treves[25] was based on the assumption of a uniaxial single-ion anisotropy ($g_2=g_3$) and a calculation of susceptibilities within the leading (classical) approximation. It turns out that the classical susceptibilities are not especially sensitive to the precise value of g_2, as long as inequalities (3.1) are enforced, which must then be determined by independent measurements such as the magnon activation frequencies[10] or the mobility ratio.[17,18] Because of the crudeness of the theoretical models used to describe a rather complex physical situation, and a corresponding uncertainty in actual experiments, it is probably fair to say that a precise knowledge of the microscopic parameters is not available at this point.

Although the emphasis in the main text was placed on orthoferrites, the 1D discrete spin model developed in this paper may prove to be more faithful to the description of rhombohedron weak ferromagnets such as $MnCO_3$ or $FeBO_3$ (iron borate). For such a purpose one must complete the model by a proper (sixth-order) single-ion anisotropy in the basal plane and then repeat the calculations of the present paper. As mentioned already, we anticipate that the mobility curve for driven Bloch walls will share with Eq. (1.1) some broad characteristics, such as a low-field linear regime and a high-field limiting velocity c, but will differ from Eq. (1.1) in its important details for most field values of practical interest.

Finally, there is some room for theoretical improvements even within the strict limits of the model considered here. For instance, our inability to obtain an analytical solution for driven Bloch walls in the subcritical ($h<h_c$) regime forced us to complete the picture in Fig. 9 by a direct numerical simulation. It may prove possible to study the neighborhood of the bifurcation point ($h\sim h_c$) analytically and replace the rough estimate of the critical field given in Eq. (4.7) by a more accurate value. Inclusion in our basic model of the magnetoelastic couplings mentioned in the Introduction is also a subject for further investigation.

ACKNOWLEDGMENTS

I am very grateful to Victor Bar'yakhtar for a number of discussions concerning the work reviewed in Ref. 4 as well as the current effort. The present work was supported in part by a grant from the EEC(CHRX-CT93-0332), by a bilateral Greek-Slovak research program, and by the Sossino Foundation.

APPENDIX: THE CONTINUUM LIMIT

In this appendix we provide some of the algebraic details necessary for the derivation of the extended nonlinear σ model of Sec. III. As a first step we insert the Taylor expansions (3.8) in Eqs. (3.6) to obtain

$$\frac{\partial \mathbf{A}}{\partial t}+\gamma\left(\mathbf{A}\times\frac{\partial \mathbf{A}}{\partial t}\right)=\mathbf{A}\times[-2J(\mathbf{B}-\varepsilon\mathbf{B}'+\varepsilon^2\mathbf{B}'')+2\mathbf{D}\times(\mathbf{B}-\varepsilon\mathbf{B}'+\varepsilon^2\mathbf{B}'')-g_1A_1\mathbf{e}_1-g_2A_2\mathbf{e}_2-g_3A_3\mathbf{e}_3+g_0\mu_0\mathbf{H}],$$

$$\frac{\partial \mathbf{B}}{\partial t}+\gamma\left(\mathbf{B}\times\frac{\partial \mathbf{B}}{\partial t}\right)=\mathbf{B}\times[-2J(\mathbf{A}+\varepsilon\mathbf{A}'+\varepsilon^2\mathbf{A}'')-2\mathbf{D}\times(\mathbf{A}+\varepsilon\mathbf{A}'+\varepsilon^2\mathbf{A}'')-g_1B_1\mathbf{e}_1-g_2B_2\mathbf{e}_2-g_3B_3\mathbf{e}_3+g_0\mu_0\mathbf{H}]. \quad \text{(A1)}$$

This system of equations is not yet fully consistent because it appears to mix different powers of the small parameter ε. To obtain a consistent system we proceed as in Ref. 7. An equivalent form of Eq. (A1) expressed in terms of the fields **m** and **n** of Eq. (3.9) and rationalized parameters is given by

$$\dot{\mathbf{m}}+\frac{1}{2}\varepsilon\lambda(\mathbf{m}\times\dot{\mathbf{m}}+\mathbf{n}\times\dot{\mathbf{n}})=-(\mathbf{m}\times\mathbf{n})'-\varepsilon(\mathbf{m}\times\mathbf{m}'-\mathbf{n}\times\mathbf{n}')'+[\mathbf{n}\times(\mathbf{d}\times\mathbf{m})-\mathbf{m}\times(\mathbf{d}\times\mathbf{n})]+\varepsilon[\mathbf{n}\times(\mathbf{d}\times\mathbf{n}')-\mathbf{m}\times(\mathbf{d}\times\mathbf{m}')]$$
$$+\varepsilon^2[\mathbf{n}\times(\mathbf{d}\times\mathbf{m}'')-\mathbf{m}\times(\mathbf{d}\times\mathbf{n}'')]-\frac{1}{2}\varepsilon\rho^2[m_2(\mathbf{m}\times\mathbf{e}_2)+n_2(\mathbf{n}\times\mathbf{e}_2)]$$
$$-\frac{1}{2}\varepsilon[m_3(\mathbf{m}\times\mathbf{e}_3)+n_3(\mathbf{n}\times\mathbf{e}_3)]+(\mathbf{m}\times\mathbf{h}),$$

$$\varepsilon\dot{\mathbf{n}}+\frac{1}{2}\varepsilon^2\lambda(\mathbf{m}\times\dot{\mathbf{n}}+\mathbf{n}\times\dot{\mathbf{m}})=2(\mathbf{m}\times\mathbf{n})+\varepsilon(\mathbf{m}\times\mathbf{m}'-\mathbf{n}\times\mathbf{n}')+\varepsilon[\mathbf{m}\times(\mathbf{d}\times\mathbf{m})-\mathbf{n}\times(\mathbf{d}\times\mathbf{n})]-\varepsilon^2(\mathbf{n}\times\mathbf{m}''-\mathbf{m}\times\mathbf{n}'')$$
$$-\varepsilon^2[\mathbf{n}\times(\mathbf{d}\times\mathbf{m}')-\mathbf{m}\times(\mathbf{d}\times\mathbf{n}')]+\varepsilon^3[\mathbf{m}\times(\mathbf{d}\times\mathbf{m}'')-\mathbf{n}\times(\mathbf{d}\times\mathbf{n}'')]$$
$$-\frac{1}{2}\varepsilon^2\rho^2[m_2(\mathbf{n}\times\mathbf{e}_2)+n_2(\mathbf{m}\times\mathbf{e}_2)]-\frac{1}{2}\varepsilon^2[m_3(\mathbf{n}\times\mathbf{e}_3)+n_3(\mathbf{m}\times\mathbf{e}_3)]+\varepsilon(\mathbf{n}\times\mathbf{h}). \quad \text{(A2)}$$

Here the dot stands for differentiation with respect to the rationalized time variable τ of Eq. (3.10) and the prime with respect to the space variable ξ of Eq. (2.17). Simple inspection of the above equations suggests that consistency is obtained if $\mathbf{m}$ is of order ε. The second equation in Eq. (A2) then becomes, to leading order,

$$\varepsilon\dot{\mathbf{n}}=2(\mathbf{m}\times\mathbf{n})-\varepsilon(\mathbf{n}\times\mathbf{n}')-\varepsilon[\mathbf{n}\times(\mathbf{d}\times\mathbf{n})]+\varepsilon(\mathbf{n}\times\mathbf{h}) \tag{A3}$$

and the constraints reduce to those of Eq. (3.11) to within terms of order ε^2. Taking the cross product of both sides of Eq. (A3) with $\mathbf{n}$ and using the reduced constraints yields

$$\mathbf{m}=\frac{\varepsilon}{2}[-\mathbf{n}'+(\mathbf{n}\times\dot{\mathbf{n}})+(\mathbf{n}\times\mathbf{d})-\mathbf{n}\times(\mathbf{n}\times\mathbf{h})], \tag{A4}$$

which coincides with the expression for the auxiliary field given in Eq. (3.12). Finally, (A4) is inserted in the first equation (A2) to yield, after lengthy but rewarding algebra, the extended nonlinear σ model (3.13) and (3.14) which is also correct to within terms of order ε^2.

[1] I. E. Dzyaloshinskii, Sov. Phys. JETP **5**, 1259 (1957).
[2] T. Moriya, Phys. Rev. **120**, 91 (1960).
[3] T. Moriya, in *Magnetism*, edited by G. T. Rado and H. Suhl (Academic, New York, 1963), p. 85.
[4] V. G. Bar'yakhtar, M. V. Chetkin, B. A. Ivanov, and S. N. Gadetskii, *Dynamics of Topological Magnetic Solitons-Experiment and Theory* (Springer-Verlag, Berlin, 1994).
[5] N. L. Schryer and L. R. Walker, J. Appl. Phys. **45**, 5406 (1974).
[6] A. P. Malozemoff and J. C. Slonczewski, *Magnetic Domain Walls in Bubble Materials* (Wiley, New York, 1981).
[7] N. Papanicolaou, Phys. Rev. B **51**, 15 062 (1995).
[8] V. S. L'vov and I. A. Prozorova, in *Spin Waves and Magnetic Excitations*, edited by A. S. Borovic-Romanov and S. K. Sinha (North-Holland, Amsterdam, 1988), p. 233.
[9] This notation was suggested to the author by V. G. Bar'yakhtar in relation to $MnCO_3$.
[10] R. M. White, R. J. Nemanich, and C. Herring, Phys. Rev. B **25**, 1822 (1982).
[11] R. W. Wang, D. L. Mills, E. E. Fullerton, J. E. Mattson, and S. D. Bader, Phys. Rev. Lett. **72**, 920 (1994).
[12] C. Micheletti, R. B. Griffiths, and J. M. Yeomans (unpublished).
[13] B. A. Ivanov and A. K. Kolezhuk, Phys. Rev. Lett. **74**, 1859 (1995).
[14] A. F. Andreev and V. I. Marchenko, Sov. Phys. Usp. **23**, 21 (1980).
[15] S. Komineas and N. Papanicolaou (unpublished).
[16] N. Papanicolaou and T. N. Tomaras, Nucl. Phys. B **360**, 425 (1991); S. Komineas and N. Papanicolaou, Physica D **99**, 81 (1996).
[17] R. W. Shumate, J. Appl. Phys. **42**, 5770 (1971).
[18] C. H. Tsang, R. L. White, and R. M. White, J. Appl. Phys. **49**, 6052 (1978).
[19] C. H. Tsang and R. L. White, J. Appl. Phys. **49**, 6063 (1978).
[20] E. M. Gyorgy and F. B. Hagedorn, J. Appl. Phys. **39**, 88 (1968).
[21] A. K. Zvezdin, JETP Lett. **29**, 513 (1979).
[22] V. G. Bar'yakhtar, B. A. Ivanov, and A. L. Sukstanskii, Sov. Phys. JETP **51**, 757 (1980).
[23] G. M. Wysin, A. R. Bishop, and J. Oitmaa, J. Phys. C **19**, 221 (1986).
[24] E. V. Gomonai, B. A. Ivanov, V. A. L'vov, and G. K. Oksyuk, Sov. Phys. JETP **70**, 174 (1990).
[25] D. Treves, Phys. Rev. **125**, 1843 (1962).